The official bi-monthly journal of Bhabha Atomic Research Centre

BARC newsletter

Volume 377 | July-August 2021 | ISSN:0976-2108

RESEARCH ARTICLES | FEATURE ARTICLE | TECHNOLOGY DEVELOPMENT | AWARDS

This page is intentionally left blank

The official bi-monthly journal of Bhabha Atomic Research Centre

BARC newsletter

Volume 377 | July-August 2021 | ISSN:0976-2108

Bird's eye view of
Bhabha Atomic Research Centre
Mumbai

Metallic oxide layer formed at the
surface for Tin

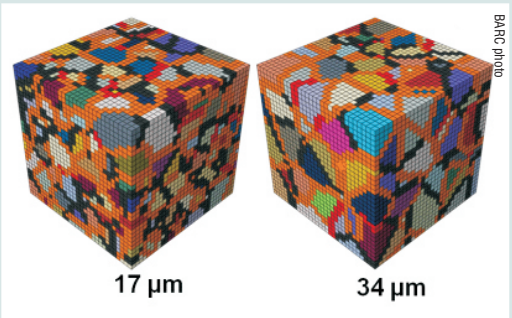

Representative Volume Elements of
different grain sizes showing
the interface elements
of alloy 690

On the Cover

Senior personnel of BARC pose for a photo in front of a newly manufactured steel forging of Reactor Pressure Vessel at a dedicated facility in Hazira, India

@ BARC Photo

This page is intentionally left blank

editor's **MESSAGE**

IAEA has recognised the radiation induced mutation breeding program of BARC with an Outstanding Achievement Award for the year 2020-21. The research program, unique to BARC, produced around 50 crop varieties with improved attributes, which were released for commercial cultivation. This issue features five articles on R&D activities in BARC. Of particular interest is the article on 2020 Nobel Prize in Chemistry. The front cover of this issue carrying the picture of a steel forging made jointly by BARC, L&T and NPCIL is a testimony to the progress made by India in this technology critical to the indigenous Pressurised Water Reactor programme of India. Finally, Research Synopsis section highlights the advances made in BARC in the use of isotope technology for groundwater management.

This page is intentionally left blank

CFD analysis of melting and evaporation of Tin in different EBVG cavities

Anik Mazumder, Sanjay Sethi*

Beam Technology Development Group,
Bhabha Atomic Research Centre, Mumbai-400 085, India

Abstract

Electron beam vapour generators (EBVG) are widely used for melting and evaporation applications of metals. Due to the high operating temperature and vacuum boundaries, often the experimental characterization of melting and evaporation of metals in EBVG cavities becomes challenging. Computational analysis provides important insights of such physical phenomena. In this study, the melting and evaporation of tin was studied in three different EBVG cavities. These cavities can accommodate a total charge volume of 30cc, 70cc and 110cc. An in-house general purpose CFD solver AnuPravaha was used for CFD simulation of melting and evaporation phenomena. The peak temperature under the e-beam, molten pool profile and evaporation rate of tin was compared for the three systems. The effect of solid metal oxide at the molten pool surface on the molten pool profile and evaporation rate was also studied. It was observed that there was marginal decrease of evaporation rate as the cavity volume was increased due to the change in convection current. The molten pool fraction increased in 70cc and 110cc cavities due to the change in aspect ratio. It was also observed that due to the presence of solid oxide on the surface, the molten fraction and the evaporation rate of tin increased marginally. The molten pool profile also changed due to the solid oxide layer. This phenomena can be attributed to the change of convection current profile at the molten metal surface.

Keywords: E-beam, Electron beam vapour generator, CFD, melting, metal evaporation

Introduction

Electron beam vapour generators (EBVG) have been extensively used for applications like physical vapour deposition (PVD), laser based isotopic purification processes (LIS) etc. [1-3]. Specially for melting and evaporation applications of high melting point and low vapour pressure metals, electron guns are often considered as the most suitable energy source owing to their high energy intensities [4-5]. Therefore, understanding the phase change phenomena of metals in the EBVG cavity has great significance for optimization of the aforementioned processes. Due to the high temperature of the system, it is often difficult to resolve the phenomena experimentally. Hence, researchers have often taken recourse to the numerical solutions along with experiments for better understanding of the system.

Melting and evaporation of different metals in electron beam gun systems has been studied extensively in literature. Westerberg and McClelland [6] has studied the effect of heat conduction and natural convection for an electron beam cold-hearth re-melting system both experimentally and with modified Galerkin finite-element method. Westerberg et al. [7] studied the evaporation of Ti and Ti-6Al-4V both experimentally and computationally and found the evaporation rate and their linear variation with e-beam power. They also observed that the computationally calculated evaporation rates were much higher than the experimentally observed value. Owing to the current focus in additive manufacturing, selective electron beam melting (SEBM) has been studied numerically using the lattice-Boltzmann method (LBM) [8, 9].

In this study, the melting and evaporation of tin have been analysed computationally with in-house developed general purpose CFD solver AnuPravaha. AnuPravaha is a finite volume solver developed in C++ platform with the capability of addressing problems from various domains of fluid flow and heat transfer [10-12]. The software has the capability of solving CFD problems over the hybrid unstructured mesh to accommodate for complex geometry without any coordinate transformation [13]. The development and experimental validation of the phase change module of AnuPravaha solver has been reported by our group elsewhere [14].

In this paper, the melting and evaporation of tin in three different EBG cavities of volume 30cc, 70cc and 110cc was studied. For laser based isotopic purification processes, the molten fraction inside the cavity is a significant process parameter [15]. Maximization of molten pool ensures the maximum participation of charge atoms in the metal vapour and increases the efficiency of isotopic purification. Hence, as an important process parameter, the molten pool fraction of tin for the three cavities were compared to access the effect of geometry on molten fraction. We also compare the maximum temperature under the electron beam and evaporation rate of tin for the three systems. Due to the high operating temperature of the system, most metallic systems in EBVG cavity consists of a surface layer of metallic oxide. During the e-beam evaporation, the oxide layer remains solid due to its high melting point. The effect of the presence of this solid oxide layer on the evaporation rate was also estimated computationally in this study.

Physical phenomena in an EBVG cavity

A general schematic of a 270° bend EBVG is shown in Figure 1. In such an EBVG system, the charge material to be evaporated is contained in a liner crucible which is placed in a water cooled copper cavity. The total system is kept inside a vacuum chamber where a chamber pressure of ~1×10^{-5} mbar is maintained

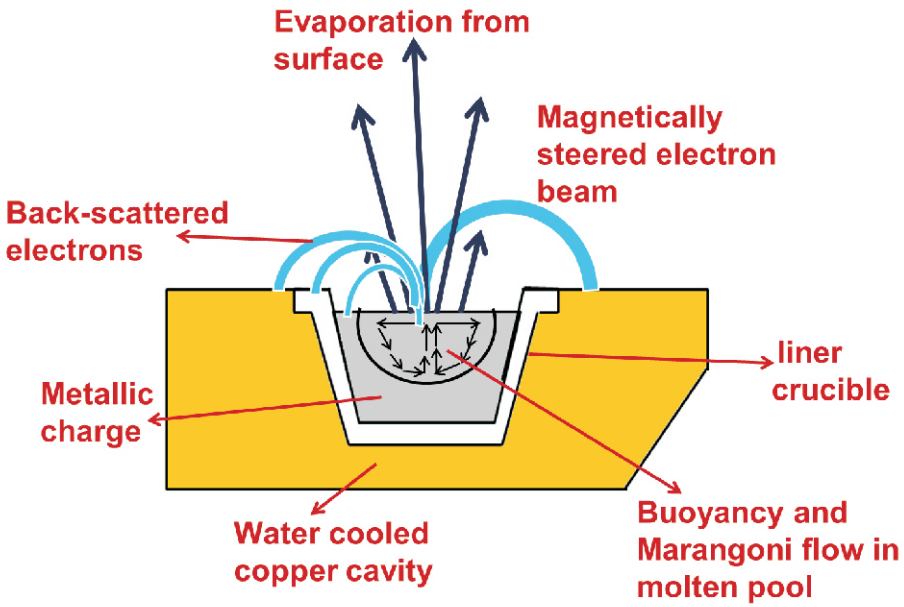

Fig. 1: Schematic of physical phenomena in EBVG cavity.

during EB operations. The electrons are generated by thermionic emission of a filament generally made of refractory metal. By virtue of an applied electric field, the electrons accelerate and form an electron beam which is then magnetically steered to the charge surface after providing a 270° bend. As the e-beam interacts with the charge metal, some fraction of the electron beam gets reflected from the surface which is referred as "back-scattered" electrons. These electrons undergo elastic collisions with the atoms of the charge. The rest of the electrons undergo inelastic collision with the charge atoms and their kinetic energy is deposited to the charge as heat. As the temperature of the surface reaches the melting temperature of the charge, the charge starts melting. As the molten pool volume increases, we observe the buoyancy driven natural convection flow in the bulk liquid. Due to the thermal gradient of surface tension, Marangoni flow can be observed at the liquid surface. Depending on the vapour pressure of the charge, evaporation of metal starts from the surface of the liquid pool when the temperature is sufficiently high. As the metal vapour leaves the liquid surface, it gives a back-thrust on the liquid surface. If the intensity of the back-thrust is significant, it can deform the liquid surface and may lead to a key-hole formation. But for applications like e-beam melting or vapour generator, the intensity of back-thrust is kept nominal and the liquid surface may be assumed to be flat.

Simulation of evaporation of tin in EBVG

The e-beam evaporation of tin inside an EBVG cavity was modelled in AnuPravaha with the following assumptions:

1. The heat flux from the electron beam was modelled as a surface heat flux with Gaussian intensity.

2. Density variation in the liquid pool was incorporated through Boussinesq approximation as the density variations in liquid metals are within the range of ±5% [16].

3. The electron beam spot was considered to be stationary.

4. Evaporation was modelled as a heat sink i.e. mass loss due to evaporation was not accounted. This assumption is valid for a quasi-steady state which is applicable where the evaporated mass is negligible compared to the total mass of the system.

5. The liquid surface was assumed to be flat and back-thrust was neglected.

6. The flow of liquid metal was assumed to be laminar.

Modelling of phase change phenomena

For modelling of the phase change phenomena for melting in the e-beam cavity, enthalpy-porosity technique [17] was used in AnuPravaha. The modelling of 2-D axis-symmetric solver for laminar flow has been described here, and a very similar approach was taken for 2-D and 3-D solvers.

Energy balance equation

For the enthalpy-porosity technique, the energy balance equation is formulated for the total enthalpy of the system. For 2-D axis-symmetric geometry, the equation is as follows

$$\rho\left(\frac{\partial h}{\partial t}+u_z\frac{\partial h}{\partial z}+u_r\frac{\partial h}{\partial r}\right)=\frac{1}{rC_p}\frac{\partial}{\partial r}\left(rk\frac{\partial h}{\partial r}\right)+\frac{1}{C_p}\frac{\partial}{\partial z}\left(k\frac{\partial h}{\partial z}\right) \quad (1)$$

In the enthalpy porosity technique, the total enthalpy gets divided into sensible enthalpy (h_s) and latent enthalpy ($h_L h$). While sensible enthalpy is used as a variable in the energy equation, the latent enthalpy is considered as a source term. It gets updated depending on the liquid fraction (f) of each cell after each time step. Simplifying equation (l) in terms of the two enthalpies finally boils down to the following

$$\frac{\partial}{\partial t}(\rho h_s)+\frac{\partial}{\partial z}(\rho u_z h_s)+\frac{\partial}{\partial r}(\rho u_r h_s)=$$
$$\frac{k}{C_p}\left(\frac{\partial^2 h_s}{\partial z^2}+\frac{\partial^2 h_s}{\partial r^2}\right)+\frac{k}{C_p}\left(\frac{\partial h_s}{\partial r}\right)-\frac{\rho u_r h_s}{r}-\rho\left(\frac{\partial h_L}{\partial t}\right) \quad (2)$$

Where the last three terms on the right hand side can be considered as source term, while the rest of the equation can be solved as 2-D energy equation.

In the source term, the latent enthalpy (h_L) is described as a function of temperature. In the case of isothermal phase change,

$h_L = f(T) = L$; when $T > T_m$

and $h_L = 0$; when $T > T_m$

where, T_m is the melting point of the solid, and L is the latent heat of enthalpy. In the enthalpy-porosity technique, the solid-liquid interface need not be tracked separately as it emerges as a part of the solution itself.

The momentum equations:

The two momentum equations for radial and axial velocity are as follows

$$\rho\left(\frac{\partial u_r}{\partial t}+u_r\frac{\partial u_r}{\partial r}+u_z\frac{\partial u_r}{\partial z}\right)=-\frac{\partial p}{\partial r}+$$
$$\mu\left[\frac{1}{r}\frac{\partial}{\partial r}\left(\frac{\partial u_r}{\partial r}\right)+\frac{\partial^2 u_r}{\partial z^2}-\frac{u_r}{r^2}\right]+S_r-Au_r \quad (3)$$

$$\rho\left(\frac{\partial u_z}{\partial t}+u_r\frac{\partial u_z}{\partial r}+u_z\frac{\partial u_z}{\partial z}\right)=-\frac{\partial p}{\partial r}+$$
$$\mu\left[\frac{1}{r}\frac{\partial}{\partial r}\left(\frac{\partial u_z}{\partial r}\right)+\frac{\partial^2 u_z}{\partial z^2}\right]+S_z-Au_z \quad (4)$$

Where, S_r and S_z contain any additional source term like buoyancy in radial and axial direction, respectively. The term A is defined as

$$A = \frac{C(1-f)^2}{f^3} \qquad (5)$$

Where "C" is the morphology constant with a large value and "f" is the liquid fraction of the cell. This term is used to differentiate between the solid and liquid phase. In the solid domain, due to its large value, the velocity is forced to zero. On the other hand, in the liquid domain, this term itself attains zero value.

The continuity equation and the other boundary conditions were implemented in a conventional way into the solver. We will discuss the implementation of concentrated beam boundary condition in details.

Surface heat flux boundary condition for electron beam

There are four different phenomena under the electron beam

1. Absorption of electron beam: after the back-scattered and transmitted particles go unused, a fraction of the total beam power is absorbed at the surface. The absorbed power was assumed to have a Gaussian profile.

2. Convection heat loss from the surface.

3. Radiation loss from the surface.

4. Evaporation loss from the surface: If the latent heat of evaporation is γ, the evaporation heat loss per unit area will be $Q_{evap} = \dot{m}\,\lambda$ Where $\dot{m}$ is the evaporative mass loss per unit area per unit time.

The evaporative mass loss can be calculated from the vapour pressure and velocity data, which will be a strong function of temperature.

Combining the four phenomena mentioned above together, we can construct an energy balance equation as follows:

$$k\frac{\partial T}{\partial n} = P_{abs} - \sigma\varepsilon(T_b^{\,4} - T_{amb}^{\,4}) - h(T_b - T_{amb}) - \lambda\dot{m} \qquad (6)$$

T_b is the boundary temperature.

T_{amb} is the ambient temperature

h is the heat transfer coefficient for convective losses along with the other conventional symbols.

We can observe that equation 6 can be written with only T_b as the unknown variable and can be solved using an appropriate root-finding algorithm. In AnuPravaha solver, Ridder's method [18] was used as the root-finding algorithm for finding the value of T_b and thereafter, the value can be used like a Dirichlet boundary.

With the aforementioned modelling approach of axis-symmetric flow and surface heat flux, the domain was discretized using the finite volume method. A pseudo-transient approach was implemented in the solver for solving both steady and unsteady problems over hybrid unstructured grid.

EBVG cavities with different volumes dimensions and boundary conditions

In this study, 3 different EBVG cavities were considered for computational analysis. The total volume of charge that can be accommodated inside these cavities are 30cc, 70cc and 110cc respectively. During the evaporation of tin, graphite crucible was used to contain the charge. A typical schematic of charge metal inside the liner crucible is shown in Fig. 2.

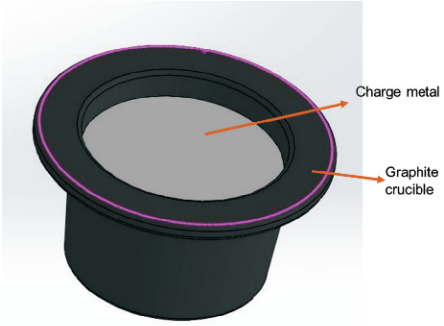

Fig. 2: Charge metal contained in a graphite crucible.

The 2D axi-symmetric view of the three EBVG systems consisting of charge and liner crucible has been shown in Fig. 3 along with the dimensions.

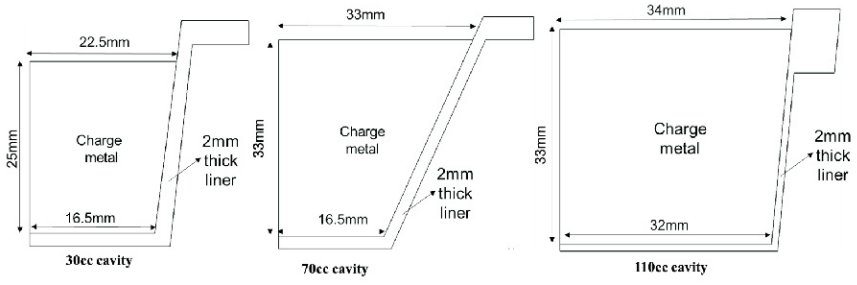

Fig. 3: 2D axi-symmetric geometry for the three EBVG cavities with dimensions.

The boundary conditions used for the numerical solution of fluid flow and heat transfer is shown in Fig, 4 for the respective boundaries.

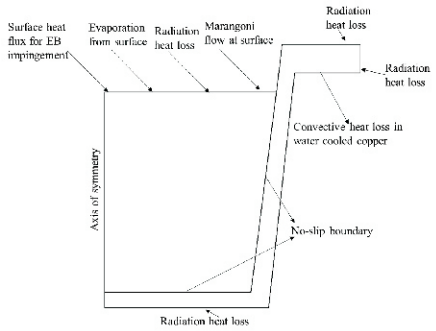

Fig. 4: The boundary conditions with the respective boundaries.

The e-beam evaporation of tin has been numerically solved for all these 3 geometries for e-beam power ranging from 1000W-1800W. The powers were selected based on the typical evaporation rates used for related applications. The temperature under the e-beam, evaporation rate of tin and molten fraction of the total charge was compared for the three systems.

Modelling the solid oxide layer on the surface of molten pool

Due to the high operating temperature of the system, the charge metal gets oxidized after repeated evaporation cycle even inside vacuum chamber. Due to their relatively high melting points, the metal oxides remain in solid phase under electron beam. As a result, two distinct zone appear at the surface of the charge. Metallic zone at the center and oxide layer at the periphery as shown in Fig. 5.

In a CFD problem, the solid oxide layer can be modelled as a "no-slip" boundary condition at the periphery. Due to this no slip boundary condition, the convection current at the surface is also likely to be changed which is likely to affect the system parameters like evaporation rate. The model is also shown in Fig. 5 in an axi-

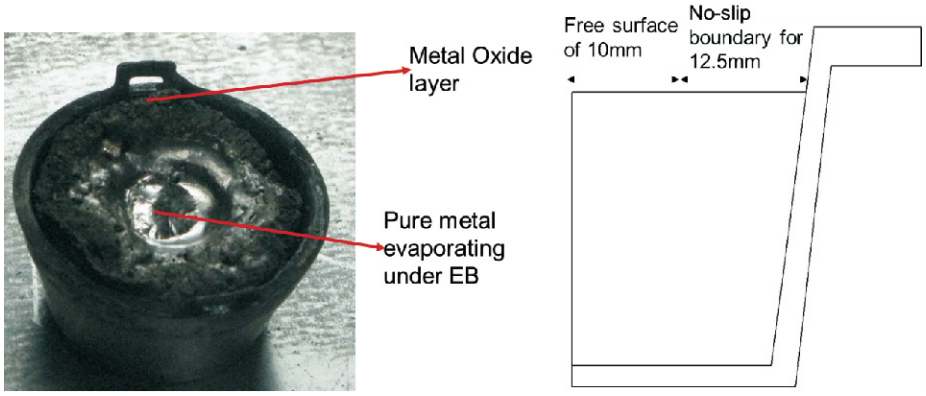

Fig. 5: An image of metallic oxide layer at the surface for tin and modelling of oxide layer as "no-slip" boundary.

symmetric domain. In this study, the molten pool profile with and without the oxide layer is compared for evaporation of tin in a 30cc cavity with 1000W EB power. The evaporation rates for both the systems were also compared.

Results and Discussions

Molten fraction of the total charge

The fraction of the total charge melted under the steady-state condition under each e-beam power was recorded. The variation of molten pool fraction for 70cc and 110cc cavity is shown in Figure 6 and Figure 7 respectively.

It was observed that the molten pool fraction does not change significantly with increasing EB power for the system under consideration in the operating range of power. The computationally obtained maximum temperature under the e-beam and the evaporation rate of tin for the three different system at different e-beam power is listed in Table 1.

From the results in Table 1, we can observe that the peak temperature and the evaporation rate reduces marginally as we increase the size of the cavity. Due to the increase of the cavity size, the distance between the heat source and heat sink changes. The change of the convection current due to this geometrical change can be identified as the reason behind the changed thermal profile. However, we can

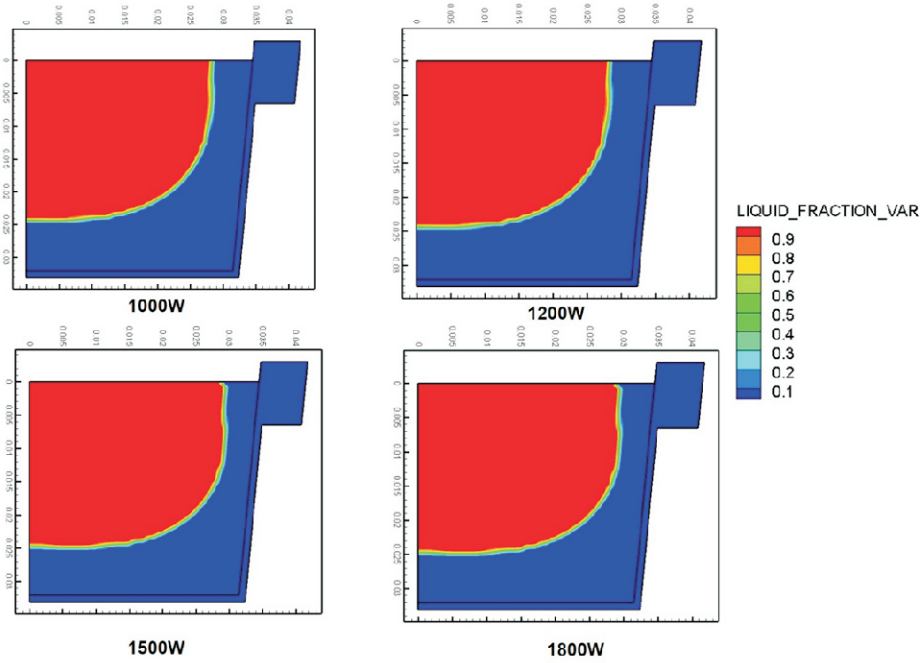

Fig. 7: Variation of molten pool fraction in 110cc cavity for 4 different EB power.

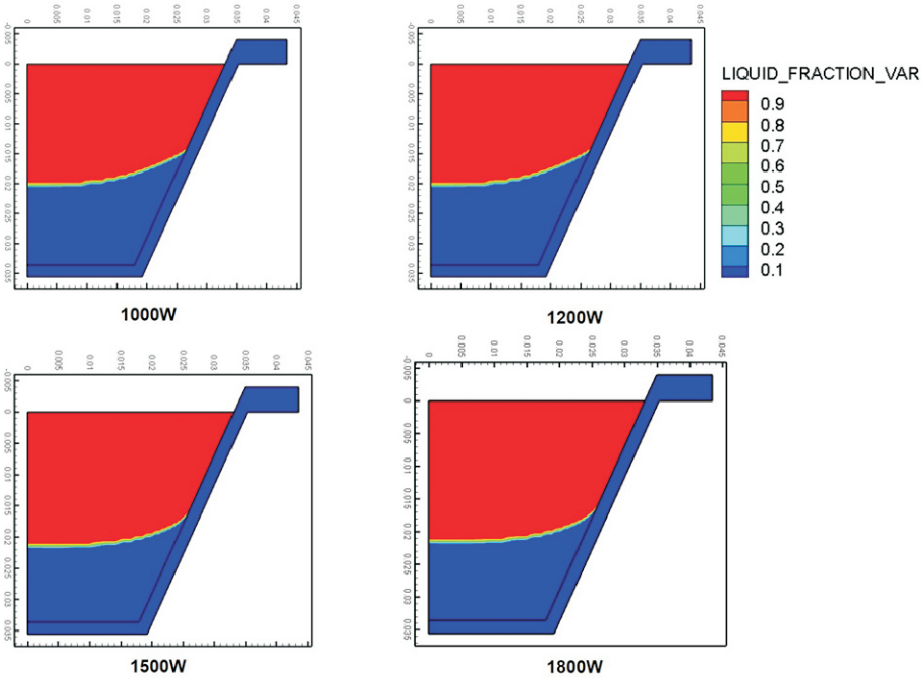

Fig. 6: Variation of molten pool fraction in 70cc cavity for 4 different EB power.

see that the molten fraction increases as we go from 30cc to 70cc and 110cc systems. Although marginal, this increase is probably due to the aspect ratio of the charge. From Fig. 6 and 7, we can identify that melting the bottom portion of the charge becomes challenging at all e-beam power. As the 30cc system has larger depth than radius, the molten fraction is relatively low. On the contrary, in 70cc and 110cc systems, the depth is nearly equal to the radius, which increases the molten fraction of the system. This phenomena can also be attributed to the change in convection current profile which assists in heat transfer to the bottom portion of the geometry in larger EBVG cavities.

Effect of oxide layer on molten pool profile and evaporation rate.

For evaporation of tin with e-beam power of 1000W, the molten pool profile

Table 1: Variation of temperature, evaporation rate and molten fraction with e-beam power at different EBVG cavities.

	Power (W)	Evaporation rate (g/h)	Maximum temperature (°C)	Molten fraction
30cc	1000	110	2345	45%
	1200	215	2468	47%
	1500	460	2610	47%
	1800	780	2700	48%
70cc	1000	100	2340	54%
	1200	212	2463	55%
	1500	450	2600	55%
	1800	750	2690	55%
110cc	1000	80	2320	56%
	1200	200	2450	57%
	1500	420	2590	58%
	1800	700	2670	58%

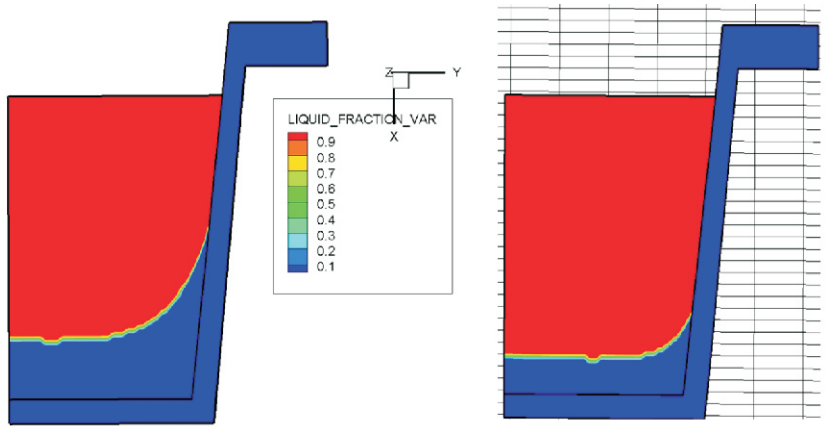

Fig. 8: Molten pool profile with free surface (no oxide layer) and 10mm free surface at center (Oxide layer in periphery).

Table 2: Comparison of computationally obtained process parameters with and without the oxide layer at surface.

Parameter	Without oxide layer	With oxide layer
Molten pool fraction	45%	49%
Peak Temperature (°C)	2345	2365
Evaporation rate (g/h)	110	130

with and without the "no-slip" oxide layer was compared. The molten pool profiles are shown in Figure 8.

The comparison of molten pool fraction, peak temperature and evaporation rates with and without the oxide layer is shown in Table 2.

From Figure 8, we can observe that the bottom profile of the molten pool changes from a parabolic shape to a flat shape in presence of solid oxide layer. From Table 2, we can also observe that the peak temperature and evaporation rate also increases in presence of oxide layer. The phenomena can be attributed to the fact that the convection current at the surface breaks down due to the solid oxide layer. Hence, the convective heat transfer to the periphery reduces. This increases the peak temperature and also increases the heat transfer to the bottom part nominally. As a result, we can observe an increase in both the molten fraction and the evaporation rate.

Conclusions

Melting and evaporation of tin in EBVG cavity was studied with an in-house general purpose CFD solver AnuPravaha. Three different EBVG cavities with different volumes were considered for analysis to estimate the effect of cavity geometry. It was observed that the evaporation rate and peak temperature under the beam reduces marginally when the cavity size increases. The change in the convection current profile was identified as the probable reason. It was also observed that, the molten pool fraction increases when the radius of the cavity is equal to or greater than the depth. Here also, the change in the convection current profile assists in the heat transfer to the bottom portion of the geometry for larger cavities. The effect of solid metal oxide layer on the melting and evaporation was also accessed with a "no-slip" boundary condition. It was observed that the molten pool profile changes due to the presence of metal oxide at the surface. The evaporation rate and molten fraction also increases marginally when the solid oxide is present in the system. This phenomena was attributed to the breakage of convection current due to solid oxide layer at the molten pool surface.

Acknowledgements

Authors acknowledge with thanks the support provided by Associate Director, Beam Technology Development Group, BARC. The authors are also thankful to Venkat P.P.K, Computer Division, BARC for providing immense support with AnuPravaha. The authors express their sincere gratitude to Prof. Amaresh Dalal, Prof Ganesh Natarajan (Mechanical Engg, IITG), Prof Arnab Atta (Chemical Engg, IIT KGP), and Nagaraj Alangi, BARC for their inputs and guidance towards this work.

Corresponding Author*

Sanjay Sethi (s_sethi@barc.gov.in)

References

[1] Rahmani, H. and Cabanas, I.L., 2019. Development of alloy coatings by electron beam physical vapour deposition method. *Surface Engineering*, pp.1-9.

[2] Ali, N., Teixeira, J.A., Addali, A., Saeed, M., Al-Zubi, F., Sedaghat, A. and Bahzad, H., 2019. Deposition of Stainless Steel Thin Films: An Electron Beam Physical Vapour Deposition Approach. *Materials*, **12(4)**, p.571.

[3] Bokhan, P.A., Buchanov, V.V., Fateev, N.V., Kalugin, M.M., Kazaryan, M.A.,

Prokhorov, A.M. and Zakrevskii, D.E., 2006. *Laser isotope separation in atomic vapor*. John Wiley & Sons.

[4] Asano, T., Uetake, N. and Suzuki, K., 1992. Mean atomic velocities of uranium, titanium and copper during electron beam evaporation. *Journal of Nuclear Science and Technology*, **29(12)**, pp.1194-1200.

[5] Schiller, S., Heisig, U. and Panzer, S., 1982. *Electron beam technology*. John Wiley & Sons.

[6] Westerberg KW, McClelland MA. Modeling of material and energy flow in an EBCHR casting system. Lawrence Livermore National Lab., CA (United States); 1994 Nov 1.

[7] Westerberg, K.W., Merier, T.C., McClelland, M.A., Braun, D.G., Berzins, L.V., Anklam, T.M. and Storer, J., 1998. Analysis of the e-beam evaporation of titanium and Ti-6Al-4V (No. UCRL-JC-128692; CONF-9710176-). Lawrence Livermore National Lab., CA (United States).

[8] Helmer, H., Bauereiß, A., Singer, R.F. and Körner, C., 2016. Grain structure evolution in Inconel 718 during selective electron beam melting. *Materials Science and Engineering*: **A**, **668**, pp.180-187.

[9] Klassen, A., Forster, V.E., Juechter, V. and Körner, C., 2017. Numerical simulation of multi-component evaporation during selective electron beam melting of TiAl. *Journal of Materials Processing Technology*, **247**, pp.280-288.

[10] Manik, J., Parmanand, M., Kotoky, S., Borgohain, P., Dalal, A. and Natarajan, G., 2017. Lessons from anupravaha: Towards a general purpose computational framework on hybrid unstructured meshes for multi-physics applications. In Proceedings of CHT-17 ICHMT International Symposium on Advances in Computational Heat Transfer. Begel House Inc..

[11] Manik, J., Dalal, A. and Natarajan, G., 2018. A generic algorithm for three-dimensional multiphase flows on unstructured meshes. *International Journal of Multiphase Flow*, **106**, pp.228-242.

[12] Parmananda, M., Dalal, A. and Natarajan, G., 2018. The influence of partitions on predicting heat transfer due to the combined effects of convection and thermal radiation in cubical enclosures. *International Journal of Heat and Mass Transfer*, **121**, pp.1179-1200.

[13] Dalal, A., Eswaran, V. and Biswas, G., 2008. A finite-volume method for Navier-Stokes equations on unstructured meshes. *Numerical Heat Transfer, Part B: Fundamentals*, **54(3)**, pp.238-259.

[14] Mazumder, A., Garg, T., Dalal, A. and Sethi, S., Development of a phase change solver for concentrated energy beam applications. (Submitted to *International communications for heat and mass transfer* in June, 2021)

[15] Mukherjee, J., Sethi, S., Anupama, P., Dey, S.P., Nagaraj, A., Das, D.R., Kumar, D., Verma, M.K., Karmakar, K., Barnwal, T.A. and Yadav, S.P., 2015. Study of condensation and flow of liquid metal for laser based purification processes. In Proceedings of the international thorium energy conference: gateway to thorium energy.

[16] Brandes, Eric A., and G. B. Brook, eds. *Smithells metals reference book. Elsevier*, 2013.

[17] Brent, A.D., Voller, V.R. and Reid, K.T.J., 1988. Enthalpy-porosity technique for modeling convection-diffusion phase change: application to the melting of a pure metal. *Numerical Heat Transfer, Part A Applications*, **13(3)**, pp.297-318.

[18] McGuire, T., 1994. Equation solving by Ridders' method. *Stata Technical Bulletin*, **3(17)**.

Simulation of deformation behavior of alloy 690

Using atomistically-informed crystal plasticity model considering effect of grain boundaries

S. Chandra, M. K. Samal*

Homi Bhabha National Institute, Mumbai - 400094, India

Abstract

In this work, the deformation behavior of alloy 690 has been predicted within the framework of crystal plasticity finite element analysis by explicitly modeling finite thickness interface elements in the polycrystalline representative volume. The work involves synergistic use of material characterization, lower scale atomistic simulations and crystal plasticity analysis. The multiscale model is further used to predict the effect of grain size on material stress-strain curve and hence, the Hall-Petch effect.

Keywords: Crystal plasticity; Grain boundary effect; Atomistic simulations; alloy 690

Introduction

The prominence of grain boundaries (GBs) in governing the deformation behavior of crystalline metals and alloys has already been established [1]. During plastic deformation, the interfaces are capable of acting as dislocation nucleation sources and sinks [1]. In a real aggregate, all these traits often occur concomitantly in conjunction with bulk plasticity. Never is this truer than in the special cases of nanocrystalline or fine grained metals and alloys, which contain a relatively high density of interfaces [2]. In addition to lattice dislocations, deformation twins are also known to emit from Gbs within the abutting grains [3]. All these deformation processes occur over a range of length and time scales and are, consequently, modeled disparately within the realm of a single length or time scale tool. The linking of scale, if done at all, is through some empirical assumptions which involves murky or unmeasurable parameters for plastic deformation. It is, therefore, desired to explore new avenues for polycrystal modeling incorporating physically justified interface modeling schemes into crystal plasticity.

In view of this, we have developed a two-scale atomistic to crystal plasticity modeling approach to simulate the deformation behavior of crystalline metals. The approach involves usage of atomistic simulations to quantify the relevant activation parameters for GBs. The extracted material parameters are directly passed on to the phenomenological flow rule of crystal plasticity model at a higher length scale. At this scale, explicit grain boundaries are modeled using three dimensional finite elements and are differentiated from bulk grains by prescribing distinct flow parameters extracted from atomistic simulations. The predictive power of the adopted methodology is accessed by performing finite element simulations of uniaxial tensile behavior of alloy 690 at quasi-static strain rates at different temperatures. In addition, the traditional Hall-Petch effect [4] (increase of flow stress with reduction in grain size) is also captured. The two-scale approach explicitly includes the effect of GBs without the involvement of arbitary constants or empirical assumptions.

Material and experiments

Alloy 690 in this work is obtained in the form of plate of dimensions 200 mm × 200 mm × 5 mm. The nominal chemical composition (wt%) of the alloy is: 60.4% Ni, 29.5% Cr, 9.38% Fe, 0.44% Si, 0.34% Mn and 0.022% C. The as-received alloy is solution annealed at 11000C for 1 hr followed by water quenching. Tensile experiments at quasi-static strain rates are carried out at different temperatures of 250°C, 1500°C, 3000°C and 6000°C. After the tensile tests, microstructural characterization using scanning electron microscope is performed to determine final grain orientations and deformed texture of the material.

Fig. 1 displays a typical EBSD map showing the grain size distribution and GB character distribution in the material. The

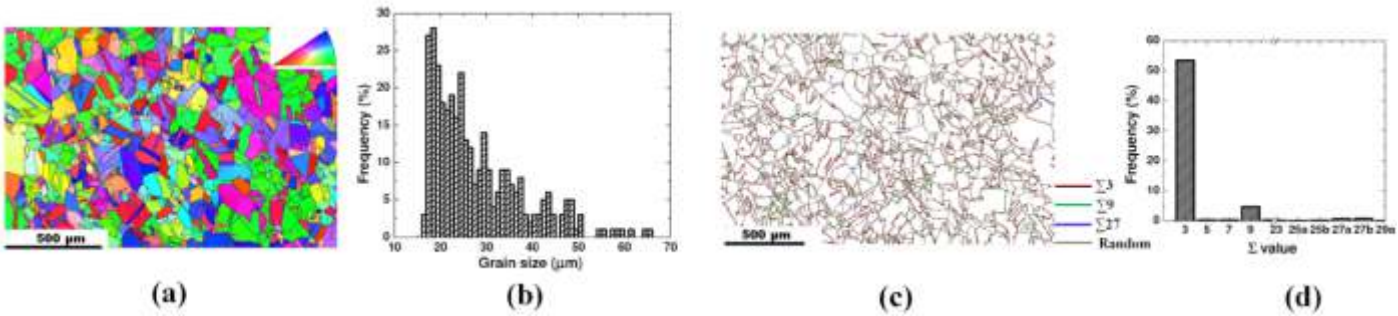

Fig. 1: (a) Initial grain orientations in alloy 690 presented by the EBSD map; (b) Initial grain size distribution; (c) GB character map and (d) distribution showing the prevalence of Σ3 boundaries in comparison to other CSL boundaries (like Σ9 or Σ27).

EBSD maps shows the prevalence of crystallographic random initial texture in the material (Fig. 1(a)). The alloy consist of equiaxed grains with an average size of 34μm (Fig.1(b)). The examination of GB character distribution map reveals that there are is a major population of Σ3 coherent twin boundaries (likely formed during annealing) and a very few higher order variants of Σ3 (like Σ9 and Σ27) boundaries (Fig. 1(c,d)). The remaining non-CSL boundaries are random boundaries (≈ 42%) which provide a connecting network to the whole EBSD map.

Fig. 2 shows that results of quasi-static tensile tests performed on alloy 690 at different temperatures. Clearly, the yield stress of the material decreases with increase in test temperature (345 MPa at 250°C, 310 MPa at 1500°C, 270 MPa at 3000°C and 220 MPa at 6000°C). A similar behavior is observed for the post yield flow stress (decrease with increasing temperature). It can, therefore, be inferred that thermally activated deformation mechanisms (dislocation motion and annihilation reactions) are the major deformation mechanisms under the investigated conditions of loading.

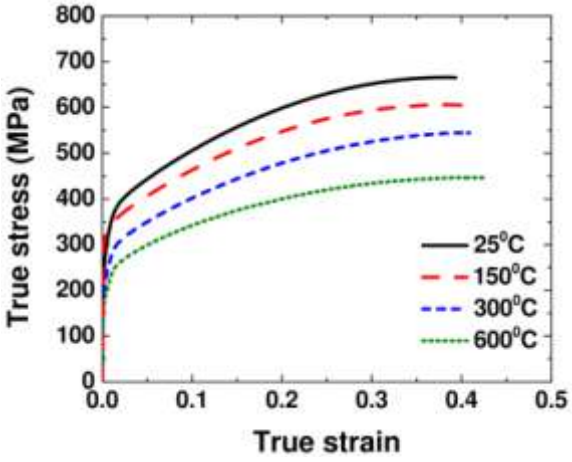

Fig. 2: Uniaxial tensile behavior of alloy 690 at different test temperatures at quasi-static strain rate.

Computational methodologies

a) Atomistics

Molecular dynamics simulations are performed using the open source code Large-scale Atomic/Molecular Massively Parallel Simulator (LAMMPS) [5] within the framework of Foiles and Hoyt [6] embedded-atom method (EAM) potential for Ni. The bicrystal models for analysis are constructed with selected orientations so as to produce Σ3 and Σ9 GBs in Ni. This is because it is observed in the EBSD scans that these two boundaries cover the major portion of the interface distribution. After checking for initial size effects and performing thermal equilibration at room temperature (300 K), the bicrystal models are subjected to uniaxial tensile loading perpendicular to the interface plane (which is oriented along y-axis). During tensile loading, microcanonical NVE ensemble is employed and velocity scaling technique is used to limit the system temperature to the desired temperature of 300 K.

Upon the application of tensile load, partial dislocation nucleation is observed in both the bicrystal models. To quantify the activation energy for this process, standard Nudged Elastic Band (NEB) calculations are performed. Specifically, these calculations take several atomic states at fixed stresses from the deformation trajectory and determines the corresponding minimum energy path at a particular value of applied stress. A total of 28 replicas are used to adequately represent the minimum energy path and the atomic states are relaxed using the fast inertial relaxation engine (FIRE) algorithm (available in LAMMPS commands) using an energy and force tolerance of 10^{-7} eV and 0.05 eV/Å, respectively, to achieve convergence.

b) Crystal plasticity simulations

The in-house crystal-plasticity based FE code CRYSP [7], developed in Reactor Safety Division, BARC, has been used in this work to perform the simulations. Within the framework of transition state theory, the embedded flow rule is given as follows [7]

$$\left|\dot{g}^{a}\right| = \begin{cases} 0, & if \left|\tau^{\alpha}_{eff}\right| \le 0 \\ \dot{\gamma}^{\alpha}_{0} \exp\left[-\frac{\Delta F}{k_B T}\left(1-\frac{\left|\tau^{\alpha}_{eff}\right|}{s^{\alpha}_{*}}\right)^{p}\right]^{q}, & if\ 0 < \tau^{\alpha}_{eff} < s^{\alpha}_{*} \end{cases} \quad (1)$$

Where $\dot{\gamma}^{\alpha}_{0}$ is reference slip rate, $\tau^{\alpha}_{\text{eff}}$ is the stress required for slip on slip system α, s* is thermal slip resistance, k_B is Boltzmann's constant, T is temperatures, ΔF is activation energy at zero stress and p and q are constants. These three parameters ($\Delta F, p, q$) are quantified from MD simulations for Σ3 and Σ9 GBs. The hardening rule is [7]:

$$\dot{s}^{\alpha} = \sum_{\beta} h^{\alpha\beta}\left|\dot{g}^{b}\right|,$$

$$h^{\alpha\beta} = [q_1 + (1 - q_1)\delta^{ab}]h^{b}_{0}\left|1 - \frac{s^{b}}{s^{b}_{s}}\right|^{r} \quad (2)$$

where $\delta^{\alpha\beta}$ is the Kronecker delta, $h^{\alpha\beta}$ is the latent hardening matrix which takes care of self as well as latent hardening of slip systems, q_1 is the latent hardening parameter, h_0 is hardening parameter, s_s is saturation slip resistance and r is the hardening exponent [7].

The Representative Volume Element (RVE) (500 μm cube consisting of 216 grains and 29,791 hexahedral finite elements with reduced integration) for alloy 690 is created using three dimensional Voronoi tessellation method. The experimentally observed initial grain size distribution (Fig. 1) and random grain orientations (using MTEX [8]) are superimposed on the RVE of alloy 690. To model finite thickness GBs, which basically represents a GB affected region (GBAR), a Java based program is developed. The program parses the input mesh file containing nodal coordinates and element-node relationship and tags the two elements as boundary elements if they share 4 nodes and belong to different grains. Thus, the GBAR in our work (by the choice of uniform meshing of the RVE) is two element thick (one element in each abutting grain). It may be noted that although the interface elements carry the

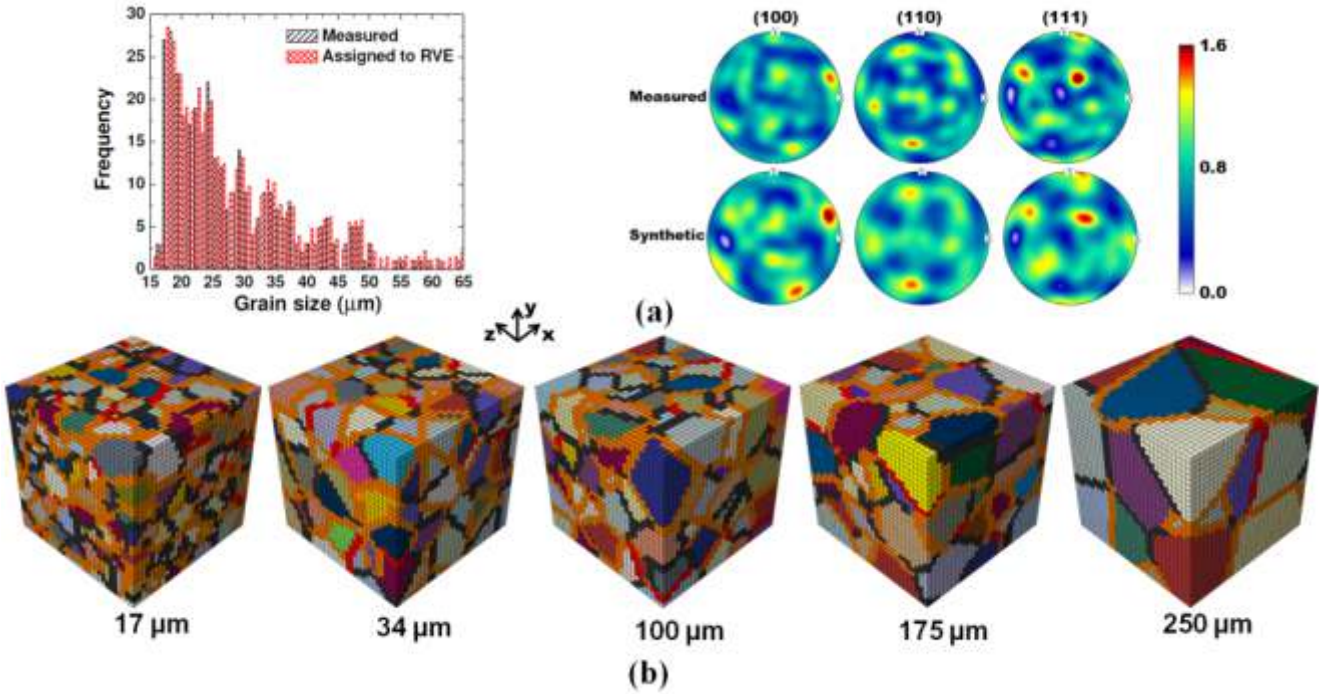

Fig. 3: (a) Initial grain orientations and texture assigned to alloy 690; (b) RVEs of different grain sizes showing the interface elements as mentioned in the text.

initial grain orientations of the abutting grains themselves, use of explicit finite elements representing the interface affected region allows us to assign distinct constitutive parameters of the crystal plasticity model to these elements.

Out of the total of 1080 interfaces present in the RVE of mean grain size 34 μm 53.4% (577 boundaries) are classified as Σ3 and 4.7% (51 boundaries) are classified as Σ9 boundaries (ignoring Σ27 boundaries). The remaining (452) boundaries are random boundaries. Similar interface character assignment is done for other volume elements of different grain sizes, which are shown in this figure, orange, red and gray color finite elements represent, respectively, Σ3, Σ9 and random interface affected regions. Uniaxial tension is applied on the RVE after imposing sufficient constraints to prevent rigid body motion.

Results and discussion

a) Atomistic simulations

NEB calculations are performed at different values of applied stress in MD simulations and the obtained results are shown in Fig. The points in figure are NEB

$$\Delta G = \Delta F \left[1 - \left(\frac{\sigma}{\sigma_c}\right)^p\right]^q \qquad (3)$$

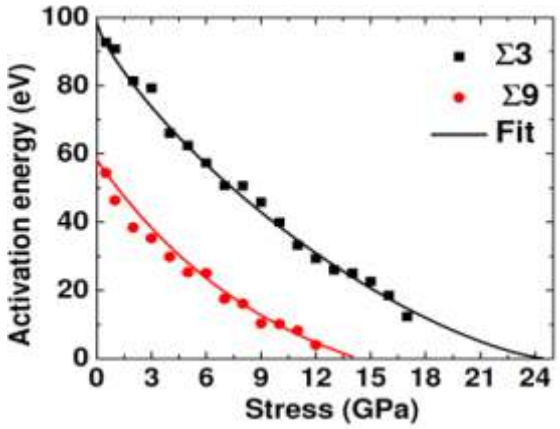

Fig. 4: Uniaxial tensile behavior of alloy 690 at different test temperatures at quasi-static strain rate.

results and solid lines are fit to the following characteristic equation, which forms the basis of flow rule of the adopted CP model:

The aforementioned fit allows us to quantify $\Delta F,p,q$ for both the GBs for use in CP simulations. The atomistically determined parameters using the NEB calculations are mentioned in Table 1.

Table 1: $\Delta F,p,q$ for Σ3 and Σ9 GBs determined from NEB calculations.

Boundary	ΔF (eV)	p	q
Σ 3	98.38	0.798	1.397
Σ 9	56.74	0.585	1.720

b) CP simulations

The CP model parameters for bulk grains of alloy 690 as well as GBs (from atomistic simulations) are mentioned in Table 2. Using these parameters, Fig. 5(a,b) displays a comparison of the experimental and CP simulation results of tensile deformation of the material at various test temperatures in the form of mechanical stress-strain curves and bulk texture evolution after deformation. A close match with the experimental data corroborates the capability of the adopted two-scale methodology in predicting the mechanical behavior of the material under the investigated conditions of loading.

Table 2: Material parameters used to simulate the mechanical behavior of alloy 690 using CP

Elastic stiffness	Constitutive parameters	Grains	Σ3 GBs	Σ9 GBs	Random GBs
C_{11} = 277 GPa	(x 10 $^{6}s^{-1}$)	6.0	6.0	6.0	6.0
C_{12} = 118 GPa	ΔF (J)	7.0×10^{-19}	15.74×10^{-18}	9.08×10^{-18}	1.75×10^{-19}
C_{44} = 79 GPa	p	0.80	0.798	0.585	0.683
	q	1.45	1.397	1.720	1.241
	q_1	1.4	1.4	1.4	1.4
	r	2.5	2.5	2.5	2.5
	s_0 (MPa)	142.0	1.0	1.0	1.0
	h_0 (MPa)	889.0	889.0	889.0	889.0
	s_s (Mpa)	406.0	406.0	406.0	406.0

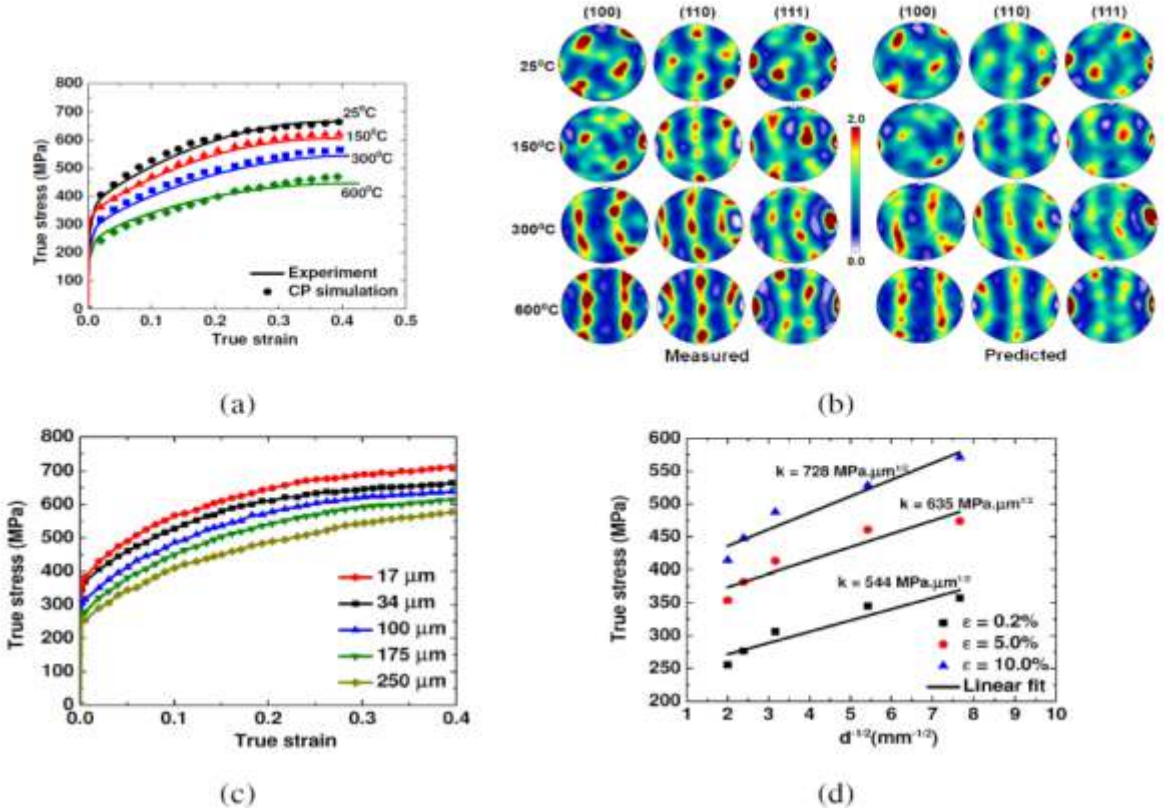

Fig. 5: Predictions of (a) tensile stress-strain curves, (b) textures at different temperatures, (c) stress-strain curves with grain sizes and (d) flow stress with grain size obtained from CP simulations of alloy 690.

In addition, the dependence of flow stress on grain size and the resulting linear HP slope [4] is also appreciably captured by the adopted methodology, as is depicted in (Fig.5 (c,d) Several interpretations can be envisioned for such observed behavior. For instance, one can cite the examples of popular pile-up models of dislocations, which were the original mechanisms used to interpret the HP effect. Within the framework of gradient plasticity theory [9], the strain incompatibility type models explain the existence of HP effect due to the existence of geometrically necessary dislocations. Another class of models relate the polycrystal to a composite [10], where the bulk grains and GBs are of different strength. The presence of relatively hard GB regions in the polycrystal leads to an increase in stress with reduction in grain size.

The dependence of flow stress of alloy 690 on grain size in this work can be directly related to the amount of GB material present in the RVE of the alloy. As can be seen from Table 2, behavior of elements corresponding to Σ3 and Σ9 GBs in our computational formulation is relatively hard (higher ΔF) ascompared to that of the bulk grains. Therefore, as the grain size reduces, the relative amount of hard material increases. Thus, smaller grain size models have a higher volume fraction of the GB elements, and thus harder material. This is the primary mechanism responsible for capturing the increase in flow stress with decrease in grain size in our CP simulations of alloy 690. In addition, the presence of GBAR may alter the dislocation mean free path. Therefore, it is clear from the aforementioned simulations that our methodology is able to predict the grain size dependence of flow stress in alloy 690 under the given conditions of loading.

Conclusions

The material stress-strain curve of alloy 690, its temperature-dependence and the influence of grain size on stress-strain curve, have been captured through a new two-scale material modeling technique, where the parameters have been transferred from atomistic scale to the crystal-plasticity length scale. Through the use of explicit interface elements for the grain boundaries, the polycrystalline response has been simulated satisfactorily through the use of FE-based in-house code CRYSP. It is envisioned that the approach can be generalized and pushed forward to include many other thermally activated GB-related deformation mechanisms. Complemented by electron microscopy, the interface makeup of the material can be determined and modeled using a RVE, thereby making this methodology very simple and convenient for persual.

Corresponding Author*

M.K. Samal (mksamal@barc.gov.in)

References

[1] J. P. Hirth, The influence of grain boundaries on mechanical properties, *Metall. Trans.* **3** (1972) 3047–3067.

[2] S. N. Naik, S. M. Walley, The Hall-Petch and inverse Hall-Petch relations and the hardness of nanocrystalline metals, *J. Mater. Sci.* **55** (2020) 2661–2681.

[3] Q. Li, L. Wang, J. Teng, X. Pang, X. Han, J. Zou, In-situ observation of cooperative grain boundary sliding and migration in the nano-twinned nanocrystalline-Au thin-films, *Scr. Mater.* **180** (2020) 97 – 102.

[4] E. Hall, *Proc. Phys. Soc.* Lond. **B 64** (1951) 747–753.

[5] S. Plimpton, Fast parallel algorithms for short-range molecular dynamics, *J. Comput. Phys.* **117** (1995) 1–19.

[6] S. M. Foiles, J. J. Hoyt, Computation of grain boundary stiffness and mobility from boundary fluctuations, *Acta Mater.* **54** (2006) 3351–3357.

[7] M. K. Samal, Development of a model for simulation of micro-twin and corresponding asymmetry in high temperature deformation behavior of nickel-based superalloy single crystals using crystal plasticity based framework, *J. Mech. Eng. Sci.* **231** (2017) 2621–2635.

[8] R. Hielscher, H. Schaeben, A novel pole figure inversion method: Specification of the MTEX algorithm, *J. Appl. Cryst.* **41** (2008) 1024–1037.

[9] J. Aldazabal, J. G. Sevillano, Hall–Petch behaviour induced by plastic strain gradients, *Mater. Sci. Eng.*, **A 365** (2004) 186–190.

[10] D. Benson, H. Fu, M. Meyers, On the effect of grain size on yield stress: extension into nanocrystalline domain, *Mater. Sci. Eng.* **A 319** (2001) 854–861.

Freeze-dried kits of DOTA-TATE sourced from in-house synthesized peptide

A formulation of ^{177}Lu-DOTA-TATE dose for administration in cancer patients

Kusum Vats, Drishty Satpati*
Radiopharmaceuticals Division
Bhabha Atomic Research Centre, Mumbai-400085, India

Abstract

^{177}Lu-DOTA-TATE is the first radiopharmaceutical that has been approved in Europe, USA and Canada for peptide receptor radionuclide therapy (PRRT) of somatostatin receptor-positive neuroendocrine tumors (NETs). Broader utilization of ^{177}Lu-DOTA-TATE in nuclear medicine centres burdened with huge volume of patients requires a rapid and robust dose formulation protocol. One of the simpler methodologies for radiopharmaceutical preparation is the use of freeze-dried kits, which are pre-assembled with sterile ingredients (peptide, buffer) and hence, reduce the number of steps and manipulations during radiolabeling. Therefore, the task of freeze-dried kit preparation for formulation of ^{177}Lu-DOTA-TATE was undertaken by Radiopharmaceuticals Division. Towards this, the peptide DOTA-TATE was indigenously synthesized manually by solid phase peptide synthesis. The peptide content was then optimized for formulation of DOTA-TATE kits. Quality checks for testing sterility, pyrogen absence and stability of the kit were performed. Several batches of kits were tested to ensure high radiochemical yield of ^{177}Lu-DOTA-TATE. The freeze-dried kits were then preliminary evaluated in patients presented with neuroendocrine tumors.

Keywords: Freeze-dried kits, ^{177}Lu, DOTA-TATE, peptide synthesis, neuroendocrine tumor, quality control

Introduction

The peptide DOTA-TATE radiolabeled with diagnostic radionuclide ^{68}Ga and therapeutic radionuclide ^{177}Lu is an established standard for imaging and treatment respectively of neuroendocrine tumors (NETs) [1-4]. Though, ^{177}Lu-DOTA-TATE (Lutathera®) has been approved by Food and Drug Administration (FDA) for treatment of NETs [5] a simpler protocol for its preparation is needed to expand the utilization across different nuclear medicine centers. Three general methods adopted at hospitals for the preparation and use of radiopharmaceuticals are: (i) *Manual (wet) radiolabeling* - preparation of radiopharmaceuticals from raw materials and radionuclide following the cumbersome radiolabeling procedure, (ii) *Freeze-dried kits*-addition of appropriate amount of radioactivity to the freeze-dried kit pre-dispensed with ligand, buffer and radical scavenger (gentisic acid, ascorbic acid), (iii) *Finished radiopharmaceutical* in readymade form.

Generally, ^{177}Lu-DOTA-TATE is prepared in hospitals by manual labeling procedure which involves preparation of buffer solution and peptide solution, followed by addition of appropriate volume of buffer for pH maintenance (pH 5) and lastly, addition of required radioactivity of $^{177}LuCl_3$ and heating for patient dose formulation. This multi-step preparation is a time consuming process and also increases scope for errors. Moreover, therapeutic radiopharmaceuticals are preparations containing high radioactivity (~100-200 mCi) and also have stringent requirement of very high radiochemical yield (> 98%). Hence, a rapid and efficient radiolabeling process with adequate safety measures, needs to be in place for ^{177}Lu-DOTA-TATE preparation [6,7]. Freeze-dried kits containing pre-dispensed ligand, buffer and other excipients in powder form are attractive, viable option for simplified radiolabeling. Kit formulation requires simple addition of appropriate amount of radioactivity followed by heating. Being an easy procedure, use of kits omits the

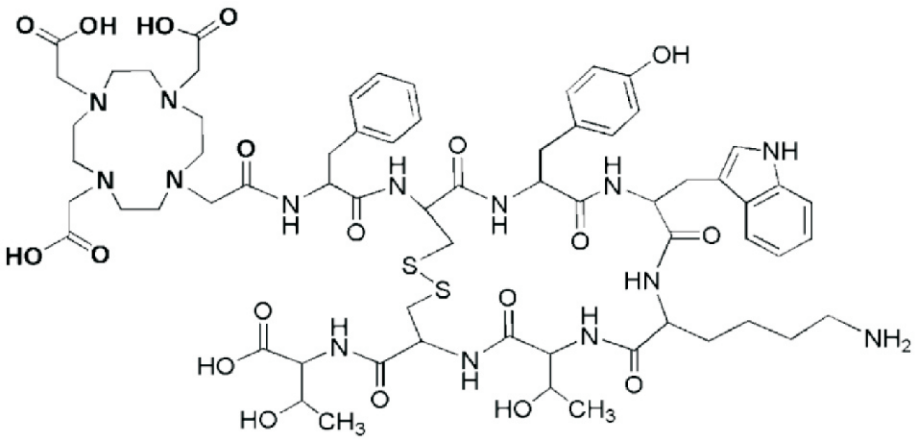

Fig.1: Chemical structure of DOTA-TATE.

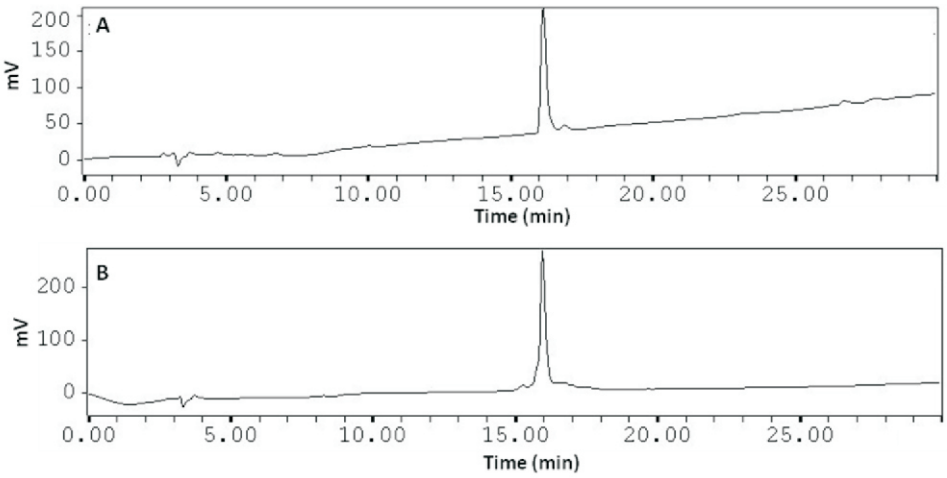

Fig.2: UV-HPLC chromatogram of (A) commercial DOTA-TATE peptide and of (B) in-house synthesized DOTA-TATE.

requirement of highly skilled personnel and the rapidity of the methodology leads to reduced radiation exposure. Despite these advantages, there are no commercial suppliers of ready-to-use freeze-dried DOTA-TATE kits for ^{177}Lu-DOTA-TATE formulation. Availability of kits will encourage more number of nuclear medicine centers to adopt the PRRT mode of treatment of NET patients.

^{177}Lu-DOTA-TATE, as a ready-to-use radiolabeled product, has been approved by Radiopharmaceutical Committee (RPC) for supply to hospitals through Board of Radiation and Isotope Technology (BRIT)/ Radiation Medicine Center (RMC). Inconsistent transportation logistics of radioactive materials is a major impediment to the use of ready radiopharmaceuticals. Geographically remote locations face troubles and transportation delays. Sometimes patients reach the nuclear medicine center for treatment after a long and difficult journey, any delay in the arrival of the radiopharmaceutical increases the waiting period and anxiety of the patient.

Preparation of ^{177}Lu-DOTA-TATE using freeze-dried kits can overcome the limitations posed by the other two methods. Hence, DOTA-TATE kits were synthesized using the in-house prepared peptide. Experiments towards optimization of kit contents were performed so as to achieve high radiochemical yield. Prepared freeze-dried kits were also supplied to a nuclear medicine hospital for therapy of patients suffering from neuroendocrine tumors.

Synthesis of DOTA-TATE

The peptide DOTA-TATE was synthesized by standard Fmoc solid phase peptide synthesis method using 2-chlorotrityl chloride resin. The fully protected peptide chain D-Phe-Cys(Acm)-Tyr(tBu)-D-Trp(Boc)-Lys(Boc)-Thr(tBu)-Cys(Acm)-Thr(tBu)-OH was prepared by successive coupling of protected amino acids using Fmoc strategy, where 3-fold excess of amino acid as well as O-(7-azabenzotriazol-1-yl)-*N,N,N',N'*-tetramethyluronium hexafluorophosphate (HATU) was used along with 6-fold excess of (N,N)-di-isopropylethylamine (DIPEA) in dimethylformamide (DMF) for 120 min. After assembling the fully protected peptide, coupling of the chelator DOTA-tris-(tBu)-ester at the N-terminus of the

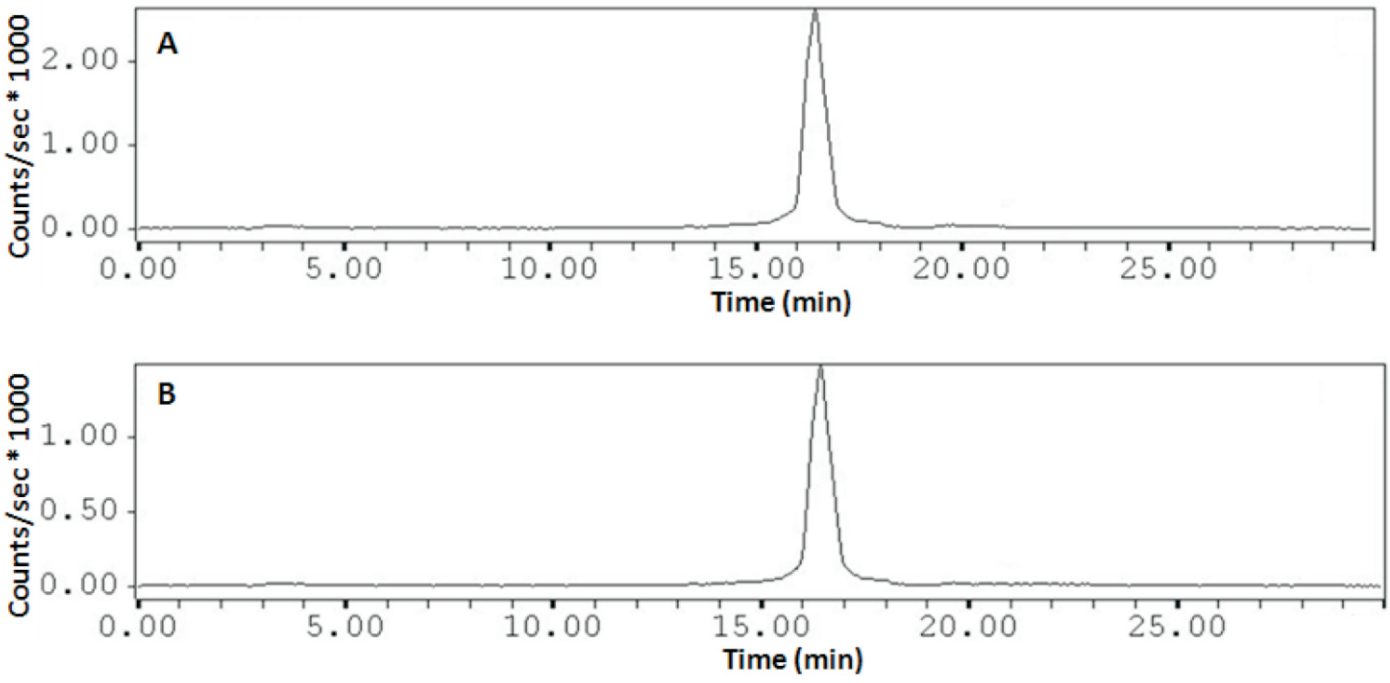

Fig.3: Radio-HPLC elution profiles of (A) ^{177}Lu-DOTA-TATE prepared using DOTA-TATE kit (B) ^{177}Lu-DOTA-TATE prepared using 1-year-old DOTA-TATE kit stored at 0°C.

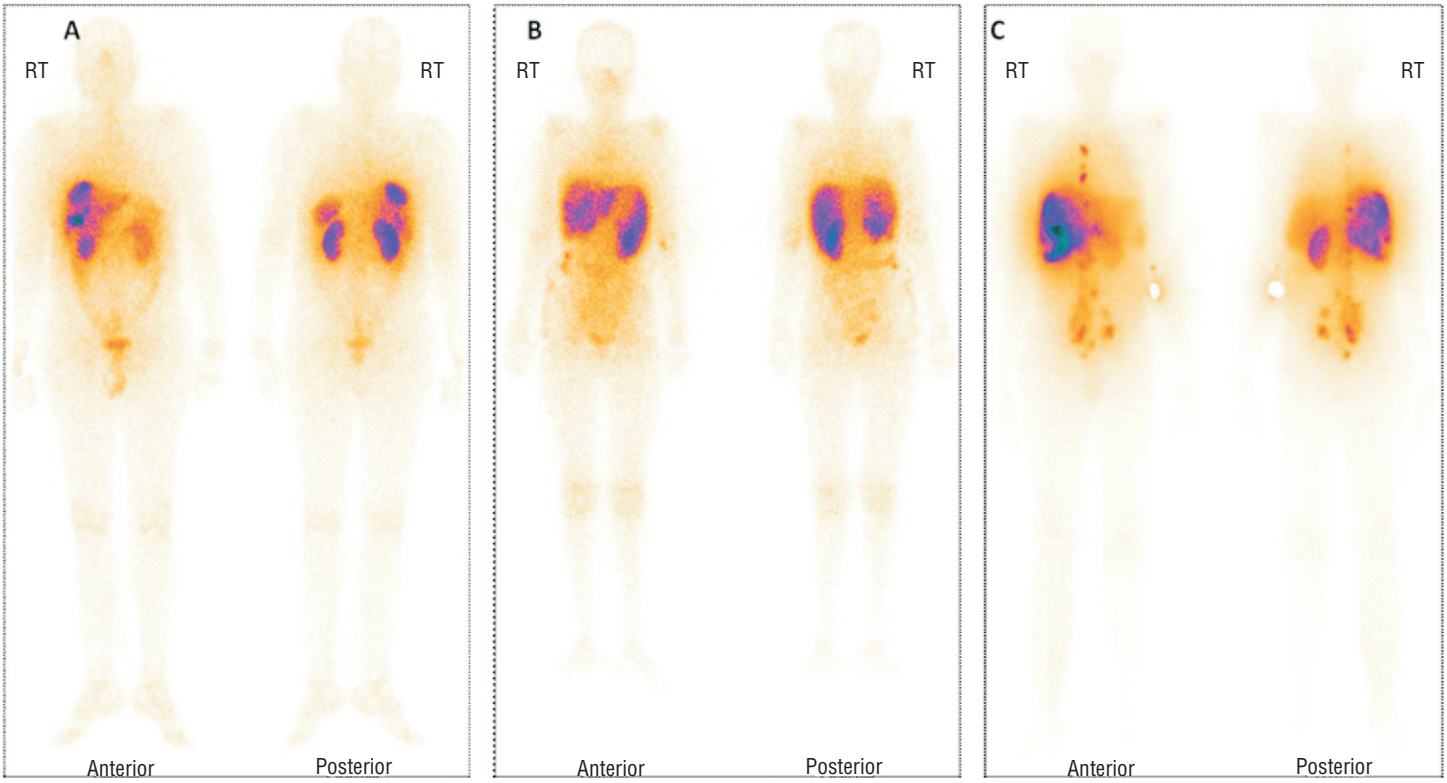

Fig.4: Whole-body scintigraphic images of kit formulated ^{177}Lu-DOTA-TATE (200 mCi) in three different patients suffering from NETs.

peptide was performed followed by on-resin cyclization with 1.2 eq. of thallium(III) trifluoroacetate in DMF. The cleavage of the peptide from the solid phase and simultaneous deprotection of side chain groups was carried out using the cocktail mixture (1 mL) of TFA/H_2O/EDT/TIPS (94:1:2.5:2.5 v/v/v/v). The crude peptide was purified by semi-preparative HPLC and characterized by mass spectroscopy. MS (ESI^+): m/z observed = 718.9 $[M+2H]^{2+}$ (calculated for $C_{65}H_{90}N_{14}O_{19}S_2$: 1434.6). The chemical structure of DOTA-TATE is presented in Fig. 1. The UV-HPLC chromatogram of in-house synthesized peptide was compared with the DOTA-TATE procured from ABX advanced biochemical compounds, GmbH (Fig. 2A & 2B).

Freeze-dried kits of DOTA-TATE

The initial radiochemical studies, carried out in order to optimize various parameters, indicated that 300 µg of DOTA-TATE is required for the formulation of patient dose of ^{177}Lu-DOTA-TATE (200 mCi) with >98% radiochemical yield using $^{177}LuCl_3$ having a minimum specific activity of 17.5 mCi/µg. Thus, each freeze-dried DOTA-TATE kit was formulated using 300 µg of DOTA-TATE peptide. Freeze-dried DOTA-TATE kits (ten numbers in each batch) were prepared according to the protocol: aqueous solution of DOTA-TATE was prepared by dissolving 3 mg of peptide in 3 mL of HPLC grade water. A solution of gentisic acid (300 mg) was prepared by dissolving it in sodium acetate buffer (0.5 M, 3 mL) by gentle warming and final pH was adjusted to ~5 by using 2 M NaOH. The peptide solution was then added to the solution of gentisic acid and the resultant solution was thoroughly mixed. The final solution was sterilized by passing through 0.22 µm Millipore filter and aliquoted into ten sterile glass vials, each vial containing 0.7 mL of the solution.

All the above procedures were carried out under aseptic conditions. Finally, the vials were frozen in dry ice at - 70˚C for 30 min and lyophilized under vacuum in a lyophilizer for 6-8 h, whereby the freeze-dried kits were obtained. Each kit vial consisted of 300 µg of DOTA-TATE, 30 mg of gentisic acid and 12.05 mg of sodium acetate. The kit vials were stored at 0˚C after lyophilization.

Kit formulation and evaluation of ^{177}Lu-DOTA-TATE

Therapeutic dose of ^{177}Lu-DOTA-TATE was prepared by addition of $^{177}LuCl_3$ (200 mCi) to the kit vial followed by addition of saline to make up the final volume of 1 mL. Subsequently, the kit was heated at 100˚C for 30 min. Radiochemical yield of ^{177}Lu-DOTA-TATE, as determined by reversed-phase high performance liquid chromatography (RP-HPLC) and paper chromatography, was >98% (Fig 3A). The radiolabeled product, ^{177}Lu-DOTA-TATE, when stored at room temperature, was observed to be stable till 3 days post reconstitution as there was no significant change in the HPLC profile.

The long term storage stability of kit vials, stored at 0˚C, was assessed by performing radiolabeling with $^{177}LuCl_3$ at periodic time intervals. The kits stored at 0˚C were found to be stable till 1 year post preparation (Fig. 3B).

The pharmacokinetics of ^{177}Lu-DOTA-TATE formulated using DOTA-TATE freeze-dried kits was studied by carrying out biodistribution studies in normal Swiss mice. ^{177}Lu-DOTA-TATE was intravenously injected into the tail vein of each mice (n = 3). Animals were sacrificed at different time intervals (3 h, 1 d, 2 d and 7 d p.i) and activity associated with each organ/tissue

was counted in flat type NaI(Tl) detector. The biodistribution study revealed rapid clearance of activity from blood and the other major organs except kidneys. More than 80% of injected activity got excreted out within 3 h p.i. and preferential route of excretion was observed to be renal pathway.

DOTA-TATE kits were clinically evaluated on formulation with $^{177}LuCl_3$ at Sri Venkateswara Institute of Medical Sciences (SVIMS, Tirupati). Therapeutic dose of ^{177}Lu-DOTA-TATE was prepared by addition of 200 mCi of $^{177}LuCl_3$ for radiotherapy of patients suffering from neuroendocrine cancers. Three doses using three kits were prepared and injected in patients presented with well differentiated NET's and associated metastasis. Single photon emission computed tomography (SPECT)/ computed tomography (CT) images in patients indicated high uptake of kit-formulated ^{177}Lu-DOTA-TATE in primary as well as metastatic sites (Fig. 4).

Conclusion

Single vial freeze-dried kits of DOTA-TATE, containing in-house synthesized DOTA-TATE peptide, were developed and successful formulation of therapeutic dose of ^{177}Lu-DOTA-TATE (200 mCi) was demonstrated. ^{177}Lu-DOTA-TATE could be prepared with >98% radiochemical purity and high stability using these kits. Preliminary clinical studies in patients suffering from NETs indicated high uptake of kit-formulated ^{177}Lu-DOTA-TATE in primary as well as metastatic sites. DOTA-TATE freeze-dried kits prepared using in-house synthesized peptide provides a convenient and cost-effective alternative for facile preparation of ^{177}Lu-DOTA-TATE in clinical setting.

Corresponding Author*

Drishty Satpati (drishtys@barc.gov.in)

Acknowledgements

The authors are thankful to Dr. Anupam Mathur of BRIT for performing mass spectroscopy. The help provided by Dr. H. D.Sarma in performing bio distribution studies is being thankfully acknowledged. The authors are also thankful to Dr. T. C. Kalawat, SVIMS, Tirupati for carrying out the clinical evaluation studies.

References

[1] Mojtahedi A.,Thamake S., Tworowska I., Ranganathan D., Delpassand E. S. The value of ^{68}Ga-DOTATATE PET/CT in diagnosis and management of neuroendocrine tumors compared to current FDA approved imaging modalities: a review of literature. *Am J Nucl Med Mol Imaging*,**4**, 2014, 426-434.

[2] Kam B.L., Teunissen J.J., Krenning E. P., de Herder W. W., Khan S., van Vliet E.I., Kwekkeboom D.J. Lutetium-labelled peptides for therapy of neuroendocrine tumours. *Eur J Nucl Med Mol Imaging*, **39** Suppl 1, 2012, S103-S112.

[3] Parghane R. V., Talole S., Prabhash K., Basu S. Clinical Response Profile of Metastatic/Advanced Pulmonary Neuroendocrine Tumors to Peptide Receptor Radionuclide Therapy with ^{177}Lu-DOTATATE. *Clin Nucl Med*, **42**, 2017, 428-435.

[4] Mittra E. S. Neuroendocrine Tumor Therapy: ^{177}Lu-DOTATATE. *Am J Roentgenol*, **211**, 2018, 278-285.

[5] Hennrich U., Kopka K. Lutathera: The First FDA- and EMA- Approved. Radiopharmaceutical for Peptide Receptor Radionuclide Therapy. *Pharmaceuticals*, **12**, 114, 2019, doi:10.3390/ph12030114.

[6] Mathur A., Prashant V., Sakhare N., Chakraborty S., Vimalnath K.V., Krishna Mohan R., Arjun C., Karkhanis B., Seshan R., Basu S., Korde A., Banerjee S., Dash A., Sachdev S. S. Bulk Scale Formulation of Therapeutic Doses of Clinical Grade Ready-to-Use ^{177}Lu-DOTA-TATE: The Intricate Radiochemistry Aspects. *Cancer Biother Radiopharm*, **32**, 2017, 266 273.

[7] Breeman W. A. P., de Jong M., Visser T.J., Erion J.L., Krenning E.P. Optimising conditions for radiolabelling of DOTA-peptides with ^{90}Y, ^{111}In and ^{177}Lu at high specific activities. *Eur J Nucl Med Mol Imaging*, **30**, 2003, 917-920

An interpretation of the Cosmological Constant from the Physical Constants

K. K. Singh*

Astrophysical Sciences Division
Bhabha Atomic Research Centre, Mumbai-400 085, India

Abstract

The simplest formulation of the present Universe is given by the Λ-Cold Dark Matter (Λ-CDM) model, where Λ being referred to as cosmological constant. In this model, the dominant energy budget of the Universe is described by the cold dark matter and the dark energy. The gravitational behavior of the dark energy for the expanding Universe is attributed to Λ which is equivalent to the vaccum energy density. The discovery of accelerated expansion of the Universe has opened the most important window not only in modern cosmology but also for the fundamental physics. In this work, we perform some analytical calculations to estimate the value of Λ using the results from the cosmological observations. The numerical value of Λ determined from cosmological observations is found to be very small, but it represents late time accelerated expansion of the Universe. Acceleration of the expanding Universe due to Λ started dominating at the epoch when age of the Universe was ~ 70% of the current age. We also discuss the unique relationship between Λ and various constants of physics derived using axiomatic approach. The numerical value of Λ derived from the physical constants is in good agreement with the value obtained from cosmological observations.

Keywords: Cosmological Constant, Dark Energy, Physical Constants, Planck Scale

Introduction

After the discovery of accelerated expansion of the Universe in 1998 from the supernovae observations [1, 2], dark energy has become one of the most attractive area of research in modern cosmology. The energy density associated with the dark energy gives rise to a negative pressure and asymptotically approaches to a constant known as cosmological constant (Λ). This cosmological constant plays an important role in explaining the observed accelerated expansion of the Universe. The dark energy through Λ is observed to contribute ~ 70% to the present cosmic budget [3]. About 26% of the cosmic budget is attributed to the cold dark matter (CDM) and rest 4% is the ordinary matter and radiation predicted by the Standard Model of partcle physics [3]. The current expansion rate of the Universe is determined by the value of Hubble constant H_0 = 70 km s^{-1} Mpc^{-1} at present epoch. This simple explanation of the present day Universe is given within the framework of so called Λ-CDM model in the modern cosmology. This model is observed to be the simplest theoretical description of the large scale evolution of the Universe as well as the astrophysical observables. However, the exact physical nature of the dark energy and constituents of the dark matter have not been clearly understood until now. A huge discrepancy is observed between the measured and theoretically estimated values of Λ [4]. Bound dark energy models have been proposed as an alternative to the Λ-CDM model for explaining the dynamics of the expanding Universe and to understand the nature of dark energy using extention of the Standard Model of particle physics [5]. Fundamental hypothesis of the standard cosmology states that the basic laws of physics remain same throughout the Universe. However, according to Dirac, constants of nature are not universal constants but they reflect the state of the Universe [6]. This indicates a possible spatial and temporal variation of the physical constants. This hypothesis motivates for investigation of speculated space-time dependence of the physical constants which can lead to a new physics. Interestingly, Λ can be expressed in terms of a few constants of physics. In this work, we investigate the relations between Λ and some constants of physics. The paper is organized as following: the constants of nature which are commonly used in astrophysics and cosmology are discussed in Section 2. In Section 3, the cosmological constant (Λ) is described. The relationship between Λ and the physical constants is discussed in Section 4. Finally, we discuss and conclude the results in Section 5.

Physical Constants

The basic laws of physics are constructed using a few constants like the speed of light in vaccum c, Planck constant h, Newtonian gravitational constant G, charge of the electron e and Boltzmann constant k_B. Combinations of these physical constants define natural units of measurement called *Planck Units*, whose magnitudes define the *Planck Scale*. The physical units at Planck scale play a very important role in cosmology to describe the early Universe and fundamental physics. The set of units at *Planck scale* are defined as follows:

- Planck length: $L_p \equiv \sqrt{\frac{G\hbar}{c^3}} = 1.6 \times 10^{-35}$ m
- Planck time: $t_p \equiv \sqrt{\frac{G\hbar}{c^5}} = 5.4 \times 10^{-44}$ s
- Planck mass: $M_p \equiv \sqrt{\frac{\hbar c}{G}} = 2.2 \times 10^{-8}$ kg
- Planck temperature: $T_p \equiv \frac{1}{k_B}\sqrt{\frac{\hbar c^5}{G}} = 1.4 \times 10^{32}$ K

where $\hbar = (\frac{h}{2\pi})$ is the reduced Planck constant. Planck length represents a lower limit to the proper distance in any space-time and quantum gravity effects become dominant at this scale hinting for search of new physics [7]. No physical instrument can be designed to measure the distances smaller than Planck length. Planck time is used to describe the sequence of events in the early Universe after the big-bang and also for the timescales associated with the quantum gravitational effects. Planck mass is used to define the primordial black holes formed in the early phases of the Universe. From the big-bang theory, the Universe has originated from very hot plasma with temperature equivalent to Planck temperature. Another important physical constant defined in the spectroscopy is the

*Fine Structure Constant (*α*)*. In terms of the physical constants, it is expressed as $\alpha \equiv \frac{e^2}{\hbar c}$ and its numerical value is measured to be 0.0072973525693 with very high precision.

Cosmological Constant

The comological constant (Λ) was introduced by Einstein in cosmology to derive the theory of a static Universe [8]. Einstein's equation for a real Universe represents relation between the curvature of spacetime and the distribution of its components and is given by:

$$G_{\mu\nu} = \frac{8\pi G}{c^4} T_{\mu\nu} + g_{\mu\nu}\Lambda \qquad (1)$$

where G_{mn} is the Eienstein's gravitational field strength tensor, T_{mn} is the energy momentum tensor which describes the distribution of the matter component in the Universe, Λ represents the dark energy component of the Universe, and g_{mn} is the metric tensor in the general theory of relativity. The physical interpretation of the Einstein's equation is *Space-time tells matter how to move; matter tells space-time how to curve.* Einstein's gravitational field equation is derived from an action and extention of the gravitational action by entering Λ does not introduce any additional degree of freedom. Λ in Equation (1) can be interpreted as energy momentum tensor for vacuum (perfect fluid) in the Universe. The energy density associated with Λ is referred to as *vacuum energy density or dark energy density* (ϵ_Λ) and it can be defined as:

$$\epsilon_\Lambda = \frac{c^4}{8\pi G}\Lambda \qquad (2)$$

The mass density (r Λ) corresponding to the vacuum energy density is expressed as:

$$\rho_\Lambda = \frac{\epsilon_\Lambda}{c^2} \qquad (3)$$

The time-component (μ = 0; ν = 0) of Einstein's equation for a flat Universe consisting of perfect fluid with non-interacting components gives Friedmann equation which is given by:

$$\frac{1}{a^2(t)}\left(\frac{da}{dt}\right)^2 = \frac{8\pi G}{3c^2}\left(\epsilon_m + \epsilon_\Lambda\right) \qquad (4)$$

where $a(t)$ is a dynamical variable known as the cosmological scale factor which determines the expansion of Universe and ϵ_m is the energy density associated with matter present in the Universe. Assuming that the Universe is dominated by the dark energy associated with Λ, dynamics of expanding Universe is given by solving Friedmann equation (Equation (4)) for $\epsilon_m \approx 0$. In this case, the scale factor is found to be:

$$a(t) \propto exp(c\sqrt{\Lambda/3}\,t) \qquad (5)$$

This indicates the expansion of the Universe for positive and nonzero cosmological constant (Λ = 0). Dimensional arguments suggest that the dimensionality of Λ should be inverse-square of distance [L^{-2}]. The acceleration of the expanding Universe is given by :

$$\frac{d^2a}{dt^2} = c^2\frac{\Lambda}{3}a(t) \qquad (6)$$

Therefore, Friedman equation derived from Einstein's field equation with Λ determines the evolution of the scale factor $a(t)$ which describes the accelerated expansion of the Universe. Also, the dark energy component of the Universe represented by Λ can be characterized as a perfect fluid with high negative pressure (p_Λ) which causes the accelerated expansion of the Universe. Hence the equation of state for dark energy should satisfy the following relation [9]:

$$p_\Lambda = -\epsilon_\Lambda \qquad (7)$$

where ϵ_Λ is given by Equation (2).

The spatial component (μ = 1; ν = 1) of Einstein's equation (Equation (1)) for a flat Universe filled with matter and dark energy gives the second Friedmann equation:

$$\frac{2}{a(t)}\frac{d^2a}{dt^2} = -\frac{8\pi G}{c^2}(p_m + p_\Lambda) - \frac{8\pi G}{3c^2}(\epsilon_m + \epsilon_\Lambda) \qquad (8)$$

where p_m is the pressure due to matter component of the Universe. Assuming that the pressure due to matter is negligible ($p_m \approx 0$) and using Equation (7) in Equation (8) we get:

$$\frac{2}{a(t)}\frac{d^2a}{dt^2} = \frac{8\pi G}{3c^2}(2\epsilon_\Lambda - \epsilon_m) \qquad (9)$$

For the static Universe, rate ($\frac{da}{dt}$) and acceleration ($\frac{d^2a}{dt^2}$) both should be zero. Therefore, if $\frac{d^2a}{dt^2} = 0$ Equation (9) reduces to

$$\epsilon_\Lambda = \frac{\epsilon_m}{2} \qquad (10)$$

Therefore, if we set $\epsilon_m = \frac{c^4}{4\pi G}\Lambda$ the set of Friedmann equations can describe the Einstein's static model of the Universe. In the context of Einstein's static Universe, it is also argued that Λ should be zero because the elements of space-time geometry depend on the energy density and pressure in the Universe [10]. In this case, the observations interpreted in terms of the accelerated expansion of the Universe can alternatively be interpreted in terms of the inhomogeneity of the Universe or extinction of light from the distant supernovae [11, 12, 13]. Also, the total energy estimation of Einstein's static homogeneous and isotropic Universe requires an infinite radius (spatially flat Universe) which results in zero cosmological constant [14]

For a flat Universe, the *critical energy density* at present epoch is defined as:

$$\epsilon_{c,0} = \frac{3c^2}{8\pi G}H_0^2 \qquad (11)$$

If the energy density is greater than $\epsilon_{c,0}$,the Universe has positive curvature and if the energy density is less than $\epsilon_{c,0}$, the Universe will be negatively curved. The numerical value of $\epsilon_{c,0}$ is estimated to be ~8.3 x 10^{-10} Joule m^{-3} and the corresponding *critical mass density* $\rho_{c,0} \sim 9.2 \times 10^{-27}$ kg m^{-3}. In cosmology, the energy density of the Universe is often expressed by a dimensionless *density parameter* (Ω) which is defined as the ratio of energy density to the critical density. Therefore, for dark energy component of the Universe associated with Λ , the density parameter is given by:

$$\Omega_\Lambda = \frac{\epsilon_\Lambda}{\epsilon_c} \qquad (12)$$

where Ω_Λ is one of the parameters in the Λ-CDM model. From the discovery of accelerated expansion of the Universe in 1998 using supernoave observations, the current value of Ω_Λ is found to be ~ 0.73 [1, 2]. Using this observed value of Ω_Λ and $\epsilon_{c,0}$ in Equation (12), the observed value of Λ is estimated to be $\Lambda_{obs} \approx 1.25 \times 10^{-52}\, m^{-2}$. Therefore, the cosmological observations suggest a positive and very small value of cosmological constant for the dark energy component of the Universe.

Relation between Cosmological Constant and Physical Constants

Assuming that the modern cosmology with Λ provides satisfactory explanation of the

Universe, two important *Cosmological scales* can be defined in the theory of gravity for cosmology. From the dimensional analysis, two physical units at *Cosmological scales* are defined as:

- Length scale: $L_\Lambda \equiv \frac{1}{\sqrt{\Lambda}}$
- Time scale: $t_\Lambda \equiv \frac{1}{c\sqrt{\Lambda}}$

The above *cosmological scales* are useful in understanding the present Universe. From the observed value of cosmological constant $\Lambda_{obs} \approx 1.25 \times 10^{-52}\ m^{-2}$ (Section 3), cosmological length and time scales are estimated to be $L_\Lambda \approx 8.7 \times 10^{25}\ m$ and $t_\Lambda \approx 9.2 \times 10^{9}$ years respectively. This indicates that the cosmological constant can influence the accelerated expansion of the Universe on large distance scales $L_\Lambda \sim 10^{25}\ m$ which is about 66 % of the Hubble radius ($\frac{c}{H_0} = 1.32 \times 10^{28}\ m$) of the present Universe. Similarly, the cosmological timescale $t_\Lambda \approx 9.2 \times 10^{9}$ years corresponds to about 70 % of the Hubble time ($\frac{1}{H_0} = 13.4 \times 10^{9}\ years$) which represents the current age of the Universe to a good approximation. Therefore, the numerical value of cosmological timescale determined from Λ_{obs} suggests late time accelerated expansion of the Universe.

Theoretical Estimation for L

Comparison of cosmological length (L_L) and time (t_L) scales with the corresponding *Planck scales* (Section 2), which are used to describe the early Universe, a huge discrepancy in their 6 numerical values (~10^{60}) is observed. Since L is associated with the fluctuations in the *vacuum energy density*, it can be theoretically derived only in the frame-work of quantum field theory. However, theoretical properties of L can be investigated from the dependence of the cosmological constant on the physical constants using axiomatic approach [15]. The four axioms for the theoretical cosmological constant (L_{theo}) are based on the following physical contents:

(I) L_{theo}theo should only depend on the physical constants in nature.

(ii) L_{theo} should have a lower bound.

(iii) Dependece of L_{theo} on the physical constants should be described in the simplest way.

(iv) Relation between L_{theo} and the physical constants should be invariant under any transformation.

On the basis of above four axioms, an explicit expression for L_{theo} is given by [15]

$$\Lambda_{theo} = \frac{G^2}{\hbar^4}\left(\frac{m_e}{\alpha}\right)^6 \qquad (13)$$

where m_e is mass of the electron (which is also a constant). Using the numerical values of the physical constants, we get $\Lambda_{theo} \approx 1.34 \times 10^{-52}\ m^{-2}$ which is consistent with the observed value of the cosmological constant (Λ_{obs}) determined from the observations as discussed in Section 3. Therefore, corresponding values of vacuum energy density (defined in Equation (2)) are in good agreement. Thus, the cosmological constant introduced by Eienstein in the gravitational field equation can be derived as a function of the physical constants using a set of physical axioms similar to information theory [16].

Effect of variations in Physical Constants on L

Dirac's hypothesis leads to the possibility of space-time variation of fundamental constants of nature [6]. Grand-Unification Theories (GUTs) in general relativity predict that Newton's gravitational constant (G) is not a universal constant but it varies as a function of low mass dynamical scalar fields [17]. From the dynamics of the Earth-Moon system, an upper-limit on the time variation of G is obtained to be [18]

$$\frac{1}{G}\frac{dG}{dt} = (0.2 \pm 0.7) \times 10^{-12}\ year^{-1} \qquad (14)$$

Some cosmological observations also provide constraints on the above value [19]. From the observation of absorption features in the optical spectra of distant quasars, evidence for cosmological evolution of (i.e redshift dependence) is reported in the literature [20, 21, 22]. In the redshift range z = 0.5 - 3.5, the time variation of fine structure constant is found to be [21, 22]:

$$\frac{\alpha - \alpha_0}{\alpha_0}\left(= -0.72 \pm 0.18\right) \times 10^{-5} \qquad (15)$$

where α_0 is the value of fine structure constant at present epoch ($z = 0$). This indicates that fine structure constant at present (α_0) has value greater than its past value (α) at nonzero redshift ($z = 0$). Modified gravity theories also predict time dependent variation of α which can break the equivalence principle in electrodynamics [23]. The equivalence principle in general theory of relativity stipulates that the gravitational acceleration of any object is independent of its mass. At *Planck scales*, the quantum gravity effects are speculated to be responsible for the Lorentz Invariance Violation (LIV) in the theory of relativity [24]. The LIV can introduce small correction to the speed of light in vacuum c at Planck energy scale ~ 10^{19} GeV. At *Cosmological scales*, matter or gravitational effect of the Universe may modify the value of c. The space-time variations of the physical constants lead to the coupling between the matter component of the Universe and massless fields [17]. Thus, the constants like G, c and α may not have universal values in the cosmological context. Therefore, the relationship between L and physical constants given by Equation (13) suggests that the cosmological constant should be time or redshift dependent. Time or redshift dependence of L is being explored through α-measurements using cosmological observations at different redshifts [25]. Models with varying L indicate presence of non-interacting dark energy and warm dark matter in the Universe [25]. Whereas, in L-CDM model, the dark energy is characterized by constant L and the dark matter is cold. Recently, the combination of multiple cosmological observations have been used to constrain the equation of state of dark energy and its energy density in the Universe [26]. In this multiprobe survey, a Universe with no dark energy component is ruled out and the geometry is found to be consistent with the spatially flat Universe. In another study, the phenomenological single-parameter dark energy parametrizations favor a phantom equation of state at present epoch [27]. A thorough investigation of dark energy using various cosmological probes is still required to understand the nature of dark energy.

Discussion and Conclusion

The dynamics of accelerating Universe indicates presence of a new component known as dark energy which dominates the late time expansion. The Universe can be described by two fundamental scales known as *Planck* and *Cosmological scales* defined by the physical constants and cosmological constant respectively. The astrophysical observations in modern cosmology show good agreement with the cosmological constant (L) interpretation

of the dark energy in the Λ-CDM model. Modern cosmology describes the structure formation and expansion dynamics of the Universe using physical models like Λ-CDM model. In such models, fundamental laws of physics play an integral role to explain the results of observational cosmology. A nonzero and positive value of Λ along with other cosmological parameters helps in understanding the slowly decaying nuclei within the current age of the Universe (~ 13.4×10^9 years) and life of old cosmic objects like white dwarfs. Any temporal or spatial deviation of Λ in general theory of relativity will lead to a new physics [28]. The *Planck scale* derived using the physical constants have important relevance for the quantum theory of gravity or simply quantum gravity. The description of Λ using various physical constants also strongly supports the interpretation of the dark energy in the modern observational cosmology. The investigation of the constancy of the physical constants provide strong motivation for new physics in modern cosmology.

Corresponding Author*

Dr. K. K. Singh (kkastro@barc.gov.in)

References

[1] Riess, A G et al. (1998) Observational Evidence from Supernovae for an Accelerating Universe and a Cosmological Constant *Astronomical Journal* **116** 1009.

[2] Perlmutter, S et al. (1999) Measurements of and from 42 *High-Redshift Supernovae Astrophysical Journal* **517** 565.

[3] Ade, P A R et al. (2016) Planck 2015 results. XIII. Cosmological parameters *Astronomy & Astrophysics* **A13** 594 .

[4] Martin, J (2012) Everything you always wanted to know about the cosmological constant problem (but were afraid to ask) *Comptes Rendus Physique* **13** 566.

[5] de la Macorra, A and Almaraz, E (2018) Theoretical and Observational Constraints of Bound Dark Energy with Precision Cosmological Data *Physical Review Letters* **121** 161303.

[6] Dirac, P A M (1937) The Cosmological Constants *Nature* **139** 323.

[7] Padmanabhan, T (1985) Physical significance of planck length *Annals of Physics* **165** 38.

[8] Einstein, A (1917) Cosmological Considerations to the General Theory of Relativity Sitzungsber Preuss Akad Wiss Berlin *(Math. Phys.)* 1 142.

[9] Peebles, P J and Ratra, B (2003) The cosmological constant and dark energy *Reviews of Modern Physics* **75** 559.

[10] Mitra, A et al. (2013) Λ CDM COSMOLOGY THROUGH THE LENS OF EINSTEIN'S STATIC UNIVERSE, THE MOTHER OF International *Journal of Modern Physics* **D 22** 1350012.

[11] Wiltshire, D L (2009) Average observational quantities in the timescape cosmology *Physical Review* **D 80** 123512.

[12] Kolb, EW(2011) Backreaction of inhomogeneities can mimic dark energy *Classical and Quantum Gravity* **28** 164009.

[13] Schild, R E and Dekker, M (2006) The transparency of the Universe limited by Ly clouds *Astronomische Nachrichten* **327** 729.

[14] Mitra, A (2013) Energy of Einstein's static universe and its implications for the Λ CDM cosmology *Journal of Cosmology and Astroparticle Physics* **03** 007.

[15] Beck, C (2009) Axiomatic approach to the cosmological constant *Physica A* **388** 3384.

[16] Abe, S (2000) Axioms and uniqueness theorem for Tsallis entropy *Physics Letters* **A 271** 74.

[17] Uzan, J P (2003) The fundamental constants and their variation: observational and theoretical status *Reviews of Modern Physics* **75** 403.

[18] Muller, J and Biskupek, L (2007) Variations of the gravitational constant from lunar laser ranging data *Classical and Quantum Gravity* **24** 4533.

[19] Ooba, J et al. (2017) Cosmological constraints on scalar–tensor gravity and the variation of the gravitational constant *Progress of Theoretical and Experimental Physics* 4 **E03** 043.

[20] Webb, J K et al. (1999) Search for Time Variation of the Fine Structure Constant *Physical Review Letters* **82** 884.

[21] Webb, J K et al. (2001) Further Evidence for Cosmological Evolution of the Fine Structure Constant *Physical Review Letters* **87** 091301.

[22] Murphy, M T et al. (2001) Possible evidence for a variable fine-structure constant from QSO absorption lines: motivations, analysis and results *Monthly Notices of the Royal Astronomical Society* **327** 1208.

[23] Hees, A et al. (2014) Breaking of the equivalence principle in the electromagnetic sector and its cosmological signatures *Physical Review* **D 90** 124064.

[24] Kosteleck´y, V A et al. (2000) Off-Shell Structure of the String Sigma Model *Physical Review Letters* **84** 4541.

[25] Wei, H et al. (2017) Cosmological constant, fine structure constant and beyond *European Physical Journal C* **77** 14.

[26] Abbott, T M C et al. (2019) Cosmological Constraints from Multiple Probes in the Dark Energy Survey *Physical Review Letters* **122** 171301.

[27] Yang, W et al. (2019) Observational constraints on one-parameter dynamical dark-energy parametriza9 tions and the H0 tension *Physical Review* **D 99** 043543.

[28] Albrecht, A et al. (2006) REPORT OF THE DARK ENERGY TASK FORCE. astro-ph/0609591.

A lab-to-land transition success story

Radiation technology for purification of Arsenic contaminated water

Nilanjal Misra, Narender Kumar Goel, Swarnima Rawat, Shubhangi A. Shelkar, Virendra Kumar*
Radiation Technology Development Division
Bhabha Atomic Research Centre, Mumbai-400085, India

Abstract

Arsenic pollution in drinking water has evolved into a critical environmental hazard in several parts of India, such as Chhattisgarh, West Bengal, Uttar Pradesh, Bihar and the northeastern region. To mitigate this problem, Radiation Technology was employed as a facile, environment friendly tool for tailoring a novel, functionalized cellulose based cationic bio-adsorbent system via radiation induced grafting process. The optimized adsorbent system was demonstrated to efficiently remove Arsenic from aqueous streams, in both batch and continuous flow mode operations. Arsenic contaminated groundwater samples collected from different affected areas were successfully treated to reduce contamination level below the WHO permissible limits of 10 ppb in drinking water. A portable water treatment setup was designed, fabricated and employed for field trials at affected areas. Post upscalation from bench to pilot scale and field trials, the technology has been successfully transferred to private licensees for point of use and point of entry water treatment applications. We have followed the concept of Technology Readiness Levels (TRLs), a method used to quantify the technical maturity of a technology throughout research, development and deployment phases.

Keywords: Arsenic, Technology Readiness Levels (TRLs), Water purification, PMAETC-*g*-Cellulose adsorbent, Radiation grafting

Introduction

Ensuring safe drinking water as an indispensable part of everyday life has been one of the foremost priorities of every country in the world. Consumption of unsafe drinking water leads to various infectious diseases, often causing fatalities. One of the major toxic water pollutants globally and a well-known carcinogen is Arsenic. Prolonged consumption of arsenic contaminated water leads to diseases such as cancer of the skin, bladder, kidney, lungs, and dermatological disorders namely, skin lesions (e.g. hyperpigmentation, hyperkeratosis), formation of rough patches on palms and soles, which are collectively termed as Arsenicosis. The World Health Organization (WHO) and the U.S. Environmental Protection Agency (USEPA) have recommended the Arsenic Maximum Contaminant Level (MCL) for public drinking water supplies to be less than 0.010 mg/L(10 ppb). In 2012, it was reported that over 200 million people worldwide are exposed to contaminated drinking water with Arsenic concentrations above 50 ppb[1]. Considering its vast population and the significant number of people that rely heavily on groundwater sources to fulfill their daily requirements, India ranks as one of the most vulnerable countries in terms of Arsenic exposure. Parts of states like West Bengal, Uttar Pradesh, Bihar, Chhattisgarh, Jharkhand, Assam, Manipur and regions mainly in the Ganga-Meghna-Brahmaputra plains have reported Arsenic levels in groundwater way above MCL values. It has been observed that drinking and cooking water along with water-soil-crop-food-transfer is the major exposure pathway for Arsenic to infiltrate the human food chain. With such a crisis looming over large sections of India's populace, the need of the hour is to provide a feasible, efficient and cost effective solution for mitigation of Arsenic contamination, both at the domestic and community levels, to evade an imminent health crisis. Conventional technologies that have been adapted over the years include use of ion exchange resins, activated charcoal, coagulation/co-precipitation, Reverse Osmosis, ultrafiltration, etc.[2-4]. But most of these methods suffer from limitations in terms of reusability, secondary waste/sludge generation, ease of operation, production process feasibility or economic viability.

The most prevalent forms of Arsenic in water are Arsenite and Arsenate. It exists in Arsenite (As(III)) form under anoxic reducing conditions, whereas Arsenate (As(V)) is prevalent in aerobic oxidizing environments, such as surface waters.[5] Moreover, the ionic forms of As(III) and As(V) depend on pH: As(V) persists in its oxyanionic forms ($H_2AsO_4^-$, $HAsO_4^{2-}$) at pH>3, while As(III) exists in its anionic form at pH>9. Hence, most of the proposed methods such as ion-exchange, adsorption, coagulation, co-precipitation, etc., display superior efficiency in removal of As(V) compared to As(III). The solution to this issue lies in pre-oxidation treatment for converting As(III) to the more easily extractable As(V) form using oxidants such as chlorine, permanganate, ozone and manganese-oxide-based solid media.[6] Therefore, it is recommended to analyze the target water quality in terms of As concentration, speciation, pH and other contaminants, in order to design an effective arsenic removal system best suited to the prevalent conditions.

Radiation Technology has been employed for the first time, to the best of our knowledge, as a facile tool for tailoring robust, recyclable functionalized cellulose

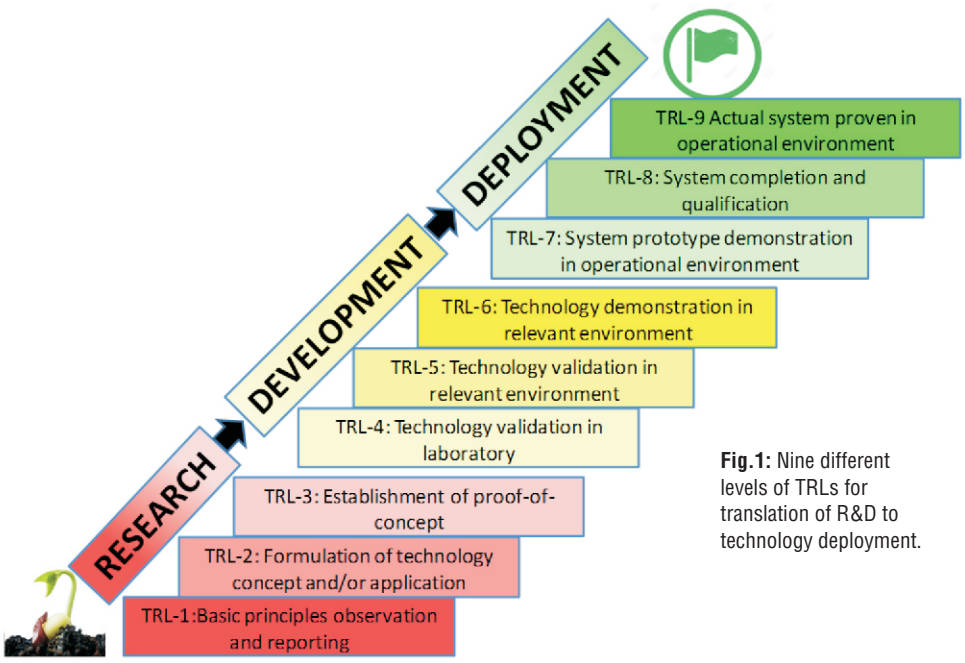

Fig.1: Nine different levels of TRLs for translation of R&D to technology deployment.

based efficient ionic bio-adsorbent for Arsenic removal from water. Post successful field trials, the scope of the work was subsequently expanded to conceptualize and materialize a unique water treatment technology for Arsenic remediation at both domestic and community levels. Throughout the evolution of this technology, we have adhered to the sequential standards demarcated under the concept of Technology Readiness Levels (TRLs), a method used to quantify the technical maturity of a technology throughout its research, development and deployment phase progression. Originally developed by NASA in the 1970s for space exploration technologies, the European Union (EU), further normalized the NASA readiness-level definitions[7], allowing for easier translation to multiple industry sectors, as presented in Fig. 1. In our scenario, the adoption of this concept has facilitated a streamlined approach towards attaining the set goals in a time bound and perspicuous manner.

Radiation induced grafting process

A single step, green synthesis of cationic cotton cellulose based adsorbent (PMAETC-*g*-cellulose) was carried out via mutual-irradiation grafting of Poly methaacryloloxyethyltrimethylammonium chloride (PMAETC), which contains a quaternary ammonium group, on to cellulose backbone using ^{60}Co-gamma radiation source[8]. The schematic of chemical modification of cellulose backbone using radiation induced graft polymerization process is illustrated in Fig. 2. Briefly, cellulose samples of predetermined weights were immersed into an optimized monomer aqueous solution in stoppered glass reactors, which were irradiated in the ^{60}Co gamma chamber (GC5000) under optimized grafting parameters. Samples were thoroughly washed to a constant weight using a soxhlet extraction assembly. This is to ensure that there is no leach out of any physically entrapped species including PMAETC homopolymer during the actual adsorption process. The grafted adsorbents were then characterized by extent of grafting, estimated gravimetrically as grafting yield (%), using the following relation (1):

$$\text{Grafting yield } (\%) = \frac{W_f - W_i}{W_i} \times 100 \qquad (1)$$

where, W_i and W_f are the weights of dry cellulose samples before and after grafting.

Basic principle and formulation of technology concept (TRL-1 & TRL-2)

The cationic groups present on radiation grafted PMAETC-g-cellulose fibrils attract the oppositely charged pollutant species present in water, followed by adsorption on the available high surface area of the cellulose adsorbent fibrils. The ionic pollutant species are removed from water through a combination of ionic interaction and adsorption processes. When the grafted polymer comes in contact with the aqueous medium, the grafted PMAETC chains form brush like structures, which offer 3D spaces for the

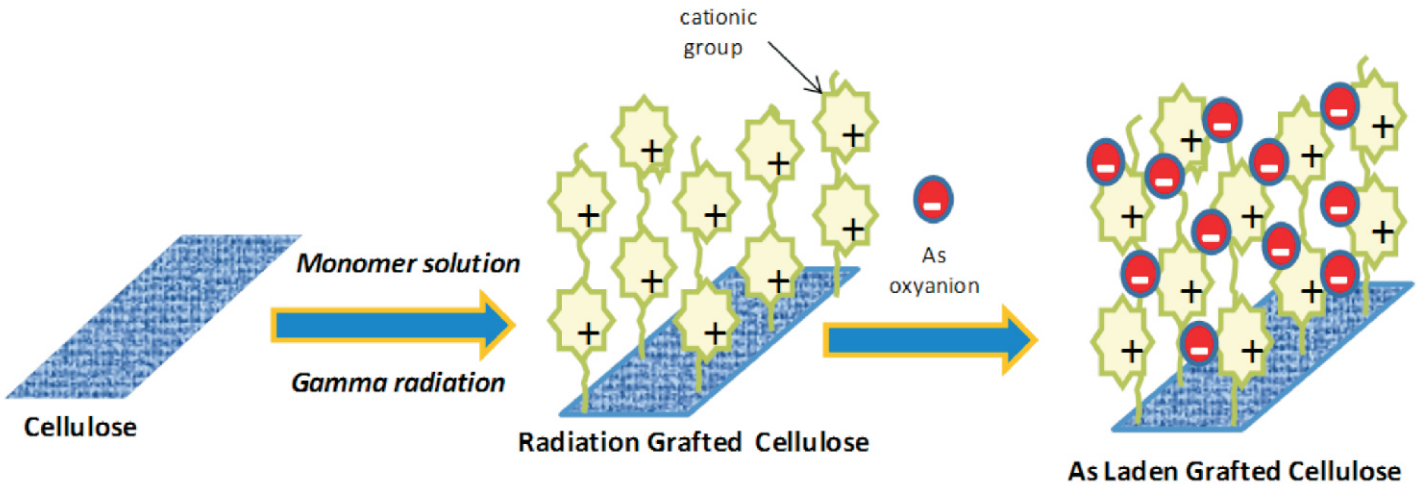

Fig.2: Schematic of radiation induced graft polymerization process and removal of Arsenic from water.

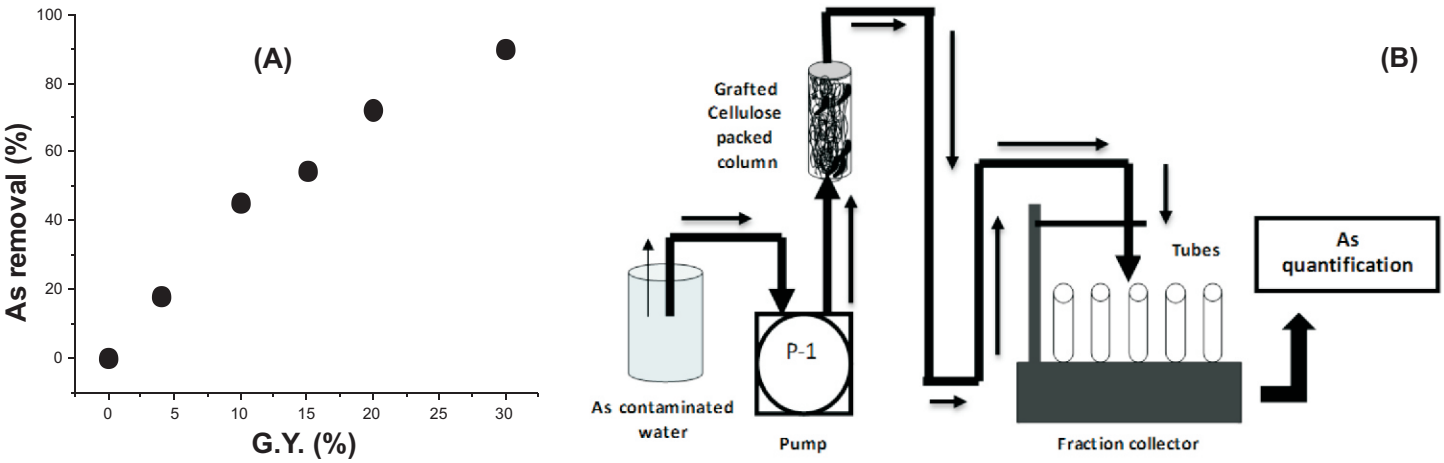

Fig.3: (A) Batch process adsorption: Arsenic removal (%) as a function of grafting yield ([As]=2.5 ppm, Adsorbent weight=10 mg, Volume=150 mL) (B) Schematic of laboratory scale fixed bed column adsorption process

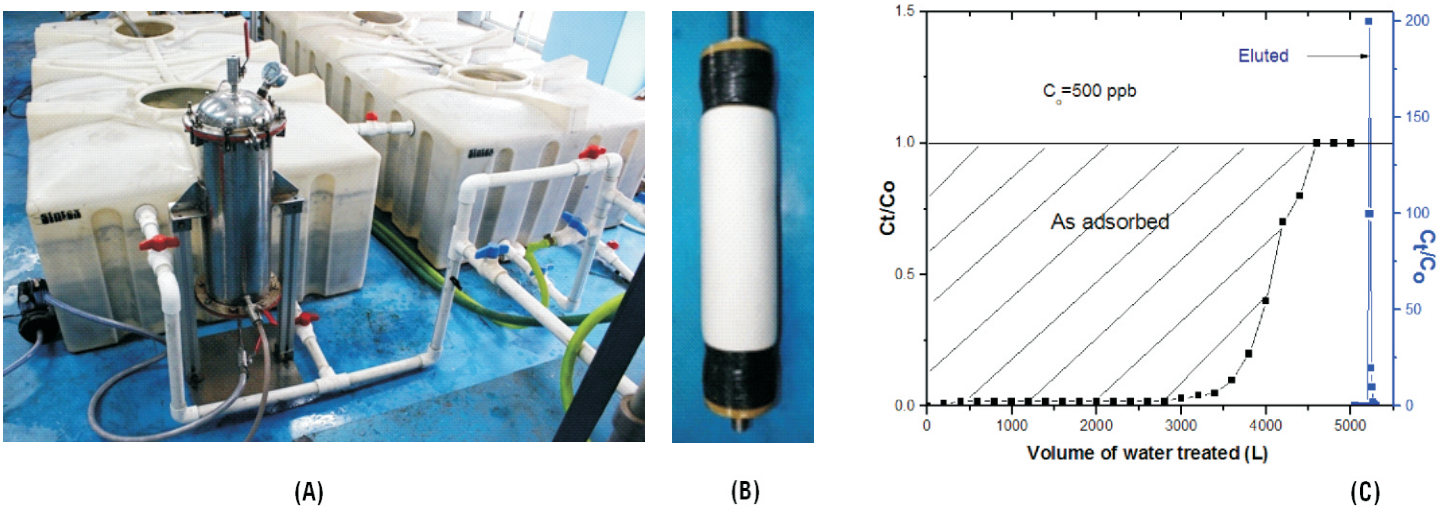

Fig.4: (A) Pilot scale study using a portable water purifier (B) Adsorbent cartridge (C) Breakthrough curve for Arsenic contaminated water ([As]=500 ppb, pH=6.5, TDS=100 ppm).

pollutant species, yielding high capacity and fast uptake kinetics (Fig. 2). The Arsenic contaminated water is pre-oxidized using sodium hypochlorite, which not only converts Arsenic (III) to Arsenic (V) but also disinfects the drinking water. The radiation grafted cellulosic adsorbent based technology is intended to remove Arsenic from water and render it safe for drinking purposes by reducing the feed concentration of over 500 ppb to less than 10 ppb, which is much lower than the limit set for Asian countries including India, i.e. 50 ppb.

The novelty of the process lies in its reusability post regeneration of the adsorbent cartridge using an optimized aqueous eluent solution, as well as in the antibacterial property of the PMAETC-*g*-Cellulose adsorbent[8]. The developed cellulose fabric based adsorbent carries brush like grafted chains containing pendent cationic groups, which can pick up negatively charged moieties. Exchange affinity is a function of net surface charge on the moieties. So the Arsenic oxyanions may have competition with other anionic species with higher surface charge (e.g., Sulphate, phosphate ions, etc.) present in the water at reasonably high concentrations. Therefore, prior to application, the water samples need to be tested to ensure that the system is conducive to removal of Arsenic (from 500 ppb to less than 10 ppb) without any significant interference from other competing species.

Establishment of proof of concept and technology validation in laboratory (TRL-3 & TRL-4)

In order to establish the proof of concept, radiation grafted bio-adsorbent was tested for removal of Arsenic from water in laboratory based batch and fixed bed column processes. For batch process studies, PMAETC-*g*-cellulose sample of a predetermined weight was equilibrated with known concentration of aqueous Arsenic (V) solution. The system was kept on stirring for ~24 hours under room temperature conditions.

The residual Arsenic (V) concentration in the solution was determined using ICP-OES (ULTIMA 2, HORIBA Scientific). The Arsenic removal (%) was found to increase almost linearly with the increase in grafting yield (Fig. 3A), which also indicated that the adsorption sites of the grafted adsorbent are readily available for the adsorbate moieties due to brush like structure of grafted chains. For regeneration and reusability of the adsorbent, an optimized aqueous eluent solution (high ionic strength aqueous solution) was used for desorption of Arsenic from the Arsenic laden adsorbent.

Fig.5: (A) Domestic Arsenic water purifier (B) Portable Arsenic water purifier for onsite field trials (C) Community level Arsenic water purifier.

For column process studies, a known weight (~1.0 g) of PMAETC-*g*-Cellulose adsorbent was packed in a cylindrical glass column (7.5 cm^3 bed volume) and an aqueous solution of Arsenic (V) passed through the fixed bed packed column under controlled flow rate using a peristaltic pump. Effluent fractions were collected at regular time intervals using a fraction collector system (Fig. 3B). Once the column gets fully saturated, the feed line was switched to the aqueous eluent solution to desorb the Arsenic from the adsorbent and regenerate it. The breakthrough curve for the complete adsorption-desorption cycle was established for multiple cycles.

A setup (Fig. 4A) was designed and fabricated for carrying out pilot scale trials and large scale technology validation at laboratory. The set up comprised of the adsorbent material (~1.0kg) wrapped as a multilayered cartridge around a perforated SS rod to collect the clean water (Fig. 4B). Arsenic contaminated water was pumped into the cartridge housing at a flow rate of 60 L/h^{-1} and the treated water collected at regular time intervals to monitor the Arsenic concentration. Over 3000L of Arsenic contaminated tap water with [As]=500 ppb (pH~6.5 to 7.5, TDS=100ppm) was successfully cleaned to safe drinking level (Arsenic <10ppb) in a single cycle. The recyclability/ regeneration of the system was also established in multiple adsorption-desorption cycles carried out by eluting the adsorbed Arsenic using the optimized eluent solution. Fig. 4C presents the breakthrough curve for complete adsorption-desorption cycle.

Technology validation in relevant environment (TRL-5)

To further validate the technology in relevant environment and on actual samples, several ground water samples were collected from affected areas of Chhattisgarh, analysed and treated using the radiation grafted cellulose adsorbent based process. The water samples were found to be severely contaminated with Arsenic, with concentration levels in the range of 200-700 ppb (pH~ 6.5 to 7.5, TDS ~100-500ppm). These samples were successfully treated in batch as well as continuous process to generate clean water with safe drinking water limits of Arsenic ([As]<10 ppb).

Technology and system prototype demonstration in relevant and operational environment (TRL-6 & TRL-7)

Depending on the scale of water treatment required, three different types of water purification prototype systems have been designed and fabricated.

a. *Gravity driven domestic level Arsenic water purifier: Suitable for small volumes of water for household drinking water purpose (Fig. 5A)*

b. *Portable Arsenic water purifier: Suitable for field trials of the technology at user sites (Fig. 5B)*

c. *Community level water purifier: Appropriate for treating large volumes of drinking water at the community level (Fig. 5C).*

A portable Arsenic water purification setup was deployed in affected villages near Raipur, Chhattisgarh and successfully demonstrated for treatment of real Arsenic contaminated bore well water samples ([As]=100 ppb to 700 ppb) (Fig. 6). For further system prototype demonstration in operational environment, the developed community level prototype treatment setup was also employed and validated for purification of Arsenic contaminated water samples. The total Arsenic concentrations in the water samples were estimated before and after treatment using Arsenic field testing kit (Merck MQuantTM 1.17927) and observed to be <10 ppb in all treated samples at site.

Technology transfer (Attaining TRL-8 and TRL-9)

To accomplish TRL-8 for system completion and qualification and TRL-9 for proving the actual system in operational environment, the technology "Cellulose

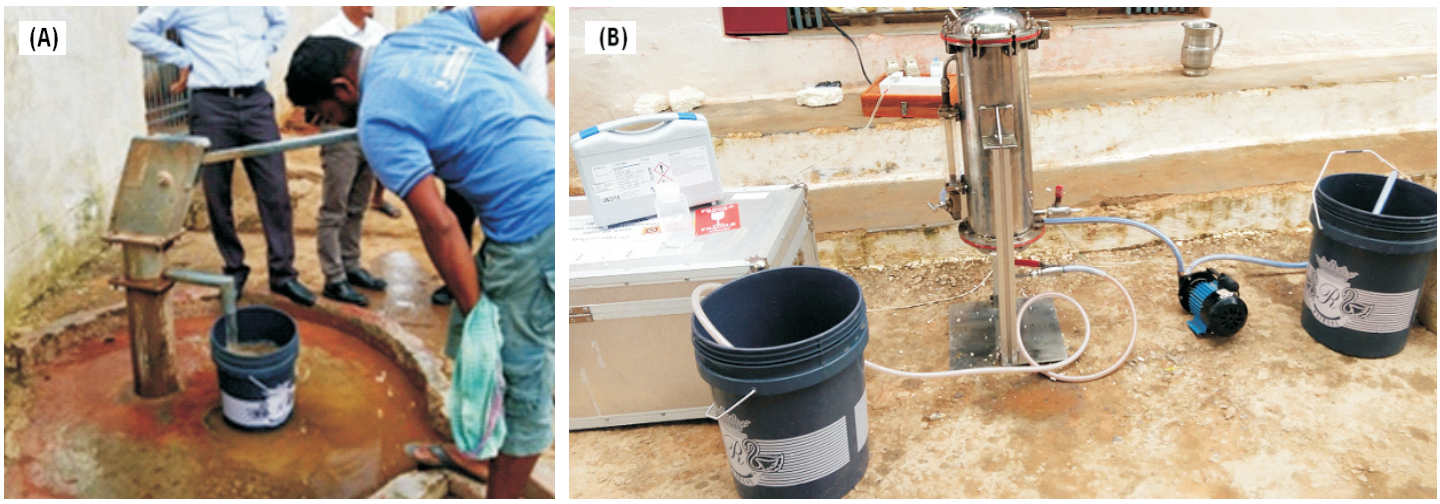

Fig.6: Field trials at an affected village near Raipur, Chhattisgarh (A) Arsenic contaminated water collected from hand pump, (B) Portable Arsenic water purifier being tested at site.

based water purifier for arsenic removal (WT21RTDD)" has been made available for transfer through TTCD, BARC. The technology has already been transferred to three licensees till date. Based on the prototype setups, the purification systems for real use in operational environment are being produced by the licensees with the requisite technical support and guidance from BARC.

Conclusion

Radiation Technology was demonstrated to be an effective tool in designing a low cost, robust and recyclable cellulosic adsorbent for Arsenic removal from water. On the basis of preliminary investigations, a prototype water treatment setup was conceptualized, designed and tested at affected sites in and around Raipur for rapid and efficient Arsenic removal from groundwater to achieve Arsenic concentration <10 ppb (WHO permissible MCL). Technology Readiness Levels (TRLs) method was followed to quantify the technical maturity of the technology. The technology has been successfully transferred to three licensees in a concerted effort towards disseminating this technical knowhow for the benefit of the people residing in regions afflicted with high Arsenic groundwater contamination.

Acknowledgement

The authors express their sincere thanks to A.R. Khaire, AMS, RTDD for technical assistance, and P.K. Pujari, Director RC&IG, Y.K. Bhardwaj, Head RTDD and L. Varshney, Ex-Head RTDD for their support and guidance.

Corresponding Author*

Virendra Kumar (vkumar@barc.gov.in)

References

[1] Murcott, S. Arsenic Contamination in the World: *An.International Sourcebook*; IWA Publishing: London, UK, 2012.

[2] Lata, Sneh; Samadder, S.R. "Removal of arsenic from water using nano adsorbents and challenges: A review". *Journal of Environmental Management*, **166**, (2016): 387-406.

[3] Nicomel, N.R.; Leus, K.; Folens, K.; Van der Voort, P; Du Laing, G. "Technologies for Arsenic Removal from Water: Current Status and Future Perspectives". *International Journal of Environmental Research and Public Health*, **13(1)**, (2016): 62.

[4] Beduk, Fatima. "Superparamagnetic nanomaterial Fe_3O_4-TiO_2 for the removal of As(V) and As(III) from aqueous solutions". *Environmental Technology*, **37(14)**, (2016): 1790-1801.

[5] WHO. Arsenic in Drinking Water; Organisation, W.H., Ed.; WHO: Geneva, Switzerland, 2011. https://www.who.int/water_sanitation_health/publications/arsenic/en/

[6] Zhang, L.; Zhu, T.; Liu, X.; Zhang, W. "Simultaneous oxidation and adsorption of As(III) from water by cerium modified chitosan ultrafine nanobiosorbent". *Journal of Hazardous Materials*, **308** (2016): 1-10.

[7] What are technology readiness levels (TRL)? https://www.twi-global.com/technical-knowledge/faqs/technology-readiness-levels.

[8] Goel, N.K.; Kumar, V.; Rao, M.S.; Bhardwaj, Y.K.; Sabharwal, S. "Functionalization of cotton fabrics by radiation induced grafting of quaternary salt to impart antibacterial property". *Radiation Physics and Chemistry*, **80**, (2011): 1233-1241.

The Journey of CRISPR-Cas

"Playing God with Life"

Dr. Devashish Rath*

The genetic material, which happens to be DNA in vast majority of organisms, is the molecular blue-print of life. The genetic code that resides as a sequence in the DNA is first copied in the form of RNA and then further translated as proteins. The proteins carry out the structural or biochemical functions in a cell. In 1953, J.D. Watson and F.H.C. Crick reported the molecular structure of DNA [1]. Ever since, scientists have tried to develop technologies that can manipulate the genetic material of cells and organisms. The genetic manipulations become increasingly complex and difficult to achieve as we move from lower organisms such as bacteria to higher organisms such as humans. Many organisms have proved genetically intractable as genetic manipulation in these remained elusive. With the discovery of the RNA-guided CRISPR-Cas9 system, an easy and effective method for genome engineering has now become a reality. The development of this technology has enabled scientists to modify DNA sequences in a wide range of cells and organisms making it possible to change the code of life. Genomic manipulations are no longer an experimental bottleneck. Today, CRISPR-Cas9 technology is used widely in basic science, biotechnology and in the development of future therapeutics [2]. French microbiologist Emanuelle Charpentier, the Director of the Max Planck Unit for the Science of Pathogens, Berlin, Germany, and the American biochemist Jennifer A. Doudna, Professor at the University of California, Berkeley, USA and Investigator, Howard Hughes Medical Institute shared the Nobel Prize in Chemistry, 2020 "for the development of a method for genome editing. The tool for genome editing came from the study of CRISPR-Cas9 system from a human pathogen named *Streptococcus pyogenes*.

The author is Group Leader, CRISPR Biology Group Applied Genomics Section, BARC

In the ensuing text I will recount the historical development of this exciting field of science, appropriately juxtaposing the contributions of the aforementioned Nobel laureates which culminated in the development of an elegant yet powerful tool for genome engineering.

The discovery of the CRISPR-Cas system in prokaryotes

Starting with the bacterium *Eschericia coli* (*E. coli*) in 1987 and in subsequent years unusual repeated elements were observed in the genomes of some bacteria. As more and more genome sequences accumulated in the databases, bioinformatics analyses revealed that such structures were common in the genomes of bacteria and these were characterized by common peculiar features: clusters of a short (about 25-50 bp), partially palindromic elements (repeats) separated by unique intervening sequences of constant length (spacers) [3-5]. Based on these features the acronym CRISPR (clustered regularly interspaced short palindromic repeats) was coined for these elements [6]. Bioinformatic analyses subsequently identified a set of genes occurring exclusively in CRISPR containing bacteria and always located adjacent to the CRISPRs aptly named as cas (CRISPR-associated) genes [6]. These genes mostly encoded proteins associated with DNA metabolism. It was also observed that CRISPR locus (repeats and spacers) gave rise to RNA called as CRISPR RNA (crRNA) but no proteins. The biological function of the CRISPR and cas genes remained a mystery until 2005, when three groups of researchers working independently reported that the unique intervening parts (spacers) of the CRISPRs were derived from bacteriophages (viruses that attack bacteria) and plasmids [7-9]. This suggested that CRISPR-cas are probably involved in protection from invading DNA such as viruses and plasmids in bacteria.

Emmanuelle Charpentier

Born 1968 in Juvisy-sur-Orge, France. Ph.D. 1995 from Institut Pasteur, Paris, France. Director of the Max Planck Unit for the Science of Pathogens, Berlin, Germany.

Jennifer A. Doudna

Born 1964 in Washington, D.C, USA. Ph.D.1989 from Harvard Medical School, Boston, USA. Professor at the University of California, Berkeley, USA and Investigator, Howard Hughes Medical Institute.

Nobel Prize Winners of 2020 (Chemistry)
"for the development of a method for genome editing"

Photo credit @ https://www.whatisbiotechnology.org/index.php/people/summary/Doudna
https://www.forbes.com/profile/emmanuelle-charpentier/?sh=3853b4027da2

CRISPR-Cas functions as an adaptable defence system

The notion that CRISPR-Cas could work as anti-virus defence was confirmed in 2007 [10] from a collaborative effort of scientists working with Danisco, a company making dairy products and scientists in academia. The Yoghurt making bacterium *Streptococcus thermophilus* (containing a class 2 CRISPR type) was infected with a virus. Resistant bacteria that survived the virus attack were isolated and their CRISPR locus was studied. The resistant bacteria had acquired new spacer sequences, which matched DNA sequence within the infecting virus. Deletion of the spacer sequence led to loss of

CRISPR and cas genes

The biological function of the CRISPR and cas genes remained a mystery until 2005, when three groups of researchers working independently reported that the unique intervening parts (spacers) of the CRISPRs were derived from bacteriophages (viruses that attack bacteria) and plasmids.

Genomic manipulations are no longer an experimental bottleneck.

Today, CRISPR-Cas9 technology is used widely in basic science, biotechnology and in the development of future therapeutics.

resistance and conversely insertion of spacer sequence in the genome of sensitive bacteria made them resistant to the virus. Furthermore, inactivation of one of the cas genes (cas9) resulted in loss of virus resistance. These experiments established two things, a) the specificity of resistance to a particular virus was dependent on the spacer sequence of the CRISPR locus and b) a gene cas9 was involved [10]. However, the molecular details of the working of the CRISPR system was still missing.

Glimpses into how the CRISPR-Cas system works came from investigations of *E. coli*, which contains a Class 1 CRISPR-Cas system comprising of eight different cas genes. Researchers led by Prof. John van der Oost at Wagingen University, Netherlands established that proteins made from five of these genes formed a multiprotein complex termed Cascade (CRISPR-associated complex for antiviral defence). Cascade was shown to cut the RNA made from the CRISPR locus inside the repeat sequence to produce shorter crRNA molecules containing the virus-derived sequence [11]. These mature crRNA molecules (having sequence complementary to viral DNA sequence) served as guide molecules that enabled Cascade assisted by another protein Cas3 to identify the infecting virus DNA and destroy it. These results suggested that CRISPR function operated in two steps: first, making of Cas proteins and processing of crRNA to mature form and formation of a complex between them, and second, an interference step in which the viral DNA was recognized and destroyed. These experiments also showed that by providing crRNA matching the viral DNA and Cas proteins a bacterium could be protected from virus attack [11].

By the year 2011, based on the work described above and work from other labs, it was realized that a number of different CRISPR-Cas systems existed in bacteria, which are now divided into two major classes [12]. In the class 1 systems, multiple Cas proteins assemble into a large CRISPR-associated complex for antiviral defence (Cascade). In contrast, class 2 systems are simpler and contain a single crRNA-binding protein (e.g. Cas9) that has all the functions necessary for viral interference. Studies had also established that the CRISPR-Cas system functioned at three different steps: (i) integration of new spacer DNA sequences into CRISPR loci (adaptation phase), (ii) processing and formation of mature crRNAs (expression phase), and (3) recognition and destruction of foreign DNA (interference phase) [13,14] (Fig. 1).

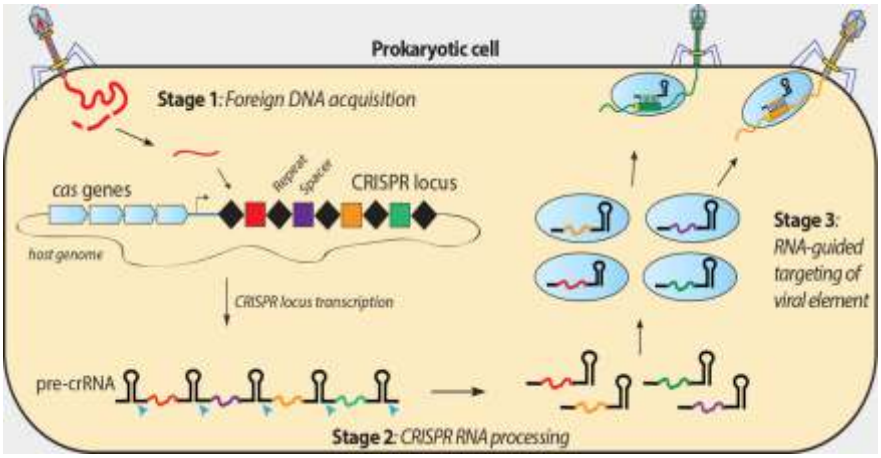

Fig. 1: A general scheme for the function of the CRISPR-Cas adaptive immune system.
Three stages are identified. Stage 1 (Adaptation): Short fragments of double-stranded DNA from a virus or plasmid are incorporated into the CRISPR array on host DNA. Stage 2(crRNA Maturation): Pre-crRNA are produced by transcription and then further processed into smaller crRNAs, each containing a single spacer and a partial repeat. Stage 3 (Interference): When crRNA recognize and specifically base-pair with a region on incoming plasmid or virus DNA the DNA is cut by associated Cas nuclease. Interference can be separated both mechanistically and temporally from CRISPR acquisition and expression.

Photo credit @ https://doudnalab.org/research_areas/crispr-systems/

Discovery of tracrRNA and its role in crRNA maturation

In 2011, Emmanuelle Charpentier and colleagues working on an infectious bacterium *Streptococcus pyogenes* [15] identified a class 2 CRISPR locus with an adjacent cas9 gene. Apart from pre-crRNA and mature crRNA they identified a small RNA species (tracrRNA) that contained a stretch of 25 nucleotides (nt) with almost perfect complementarity to the repeat regions of the CRISPR locus. Charpentier hypothesized that tracerRNA formed a duplex with pre-crRNA [15] and the structure of RNA duplex could act as processing sites for an enzyme endoribonuclease (enzyme that cuts RNA) RNase III present in the bacterium. Basically Charpentier proposed that the two RNAs are co-processed upon pairing and neither would be processed alone. The idea was proved by showing that deletion of the tracrRNA prevented pre-crRNA processing and vice versa. Further they went on to demonstrate that RNaseIII could process a heteroduplex formed between tracrRNA and pre-crRNA in vitro and was required for tracrRNA and pre-crRNA processing in vivo. Finally, they also proved that the processing required Cas9 protein. This work identified all the elements involved in crRNA maturation in a simpler

> By simply introducing an engineered sgRNA and the Cas9 nuclease, scientists are now able to make precise changes in the genome.

class 2 system and hypothesized that once processed with the help of tracrRNA the mature crRNA was sufficient to guide the cleavage of the target DNA by the Cas9 nuclease.

Towards a Genome Editing Tool

Emanuelle Charpentier collaborated with Jennifer A. Doudna to investigate if crRNA could be used to program the sequence specificity of Cas9. In other words, the idea was to provide a crRNA, that is complementary to a pre-determined target DNA, to make Cas9 recognize and cut that target in vitro. To their surprise, addition of crRNA to purified Cas9 did not result in target DNA cleavage [15,16]. After some failed experiments, in a 'eureka' moment the researchers added the tracer RNA to the in vitro reaction and it triggered the cutting of the target DNA by Cas9. Thus, the tracrRNA not only was required for pre-crRNA processing by the enzyme RNase III but was also critical for activating crRNA-guided DNA cleavage by Cas9.Through a series of biochemical experiments, the researchers showed that Cas9 had two domains and each were shown to cleave one strand of the DNA producing a double stranded break in the DNA. Further, they delineated the regions of tracrRNA and crRNA that were absolutely essential for Cas9-catalyzed cutting of the DNA through serial deletions. Based on these results the authors proceeded to simplify the system by capturing the structural features of tracrRNA and crRNA in a single molecule. Indeed, they could fuse them into a chimeric single-guide RNA (sgRNA) molecule that could act along with Cas9 (Fig.2). Finally, they also demonstrated that sgRNA sequence can be changed to make Cas9 target DNA of interest. So, they had created a simple two-component system that could be programmed by changing the sgRNA sequence to target and cut any DNA of choice (Fig.2). The importance of this finding was highlighted in the abstract of the paper where the authors wrote: “Our study reveals a family of endonucleases that use dual-RNAs for site-specific DNA cleavage and highlights the potential to exploit the system for RNA programmable genome editing” [16].

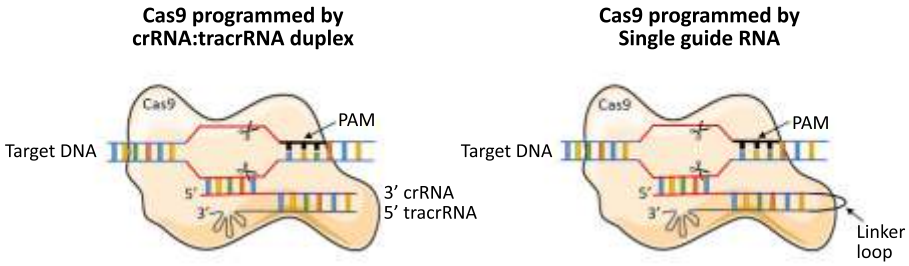

Fig. 2: Cutting of target DNA by Cas9 requires two small RNAs
crRNA (green) and tracrRNA (red). These two RNAs can be combined into a single RNA called guide RNA (gRNA) which captures structural features of both.

A Lithuanian biochemist Virginijus Siksnys and his colleagues reached similar conclusions working with the *Streptococcus thermophilus* CRISPR-Cas9 system and in fact communicated them to the journal Cell before Charpentier and Doudna, however, their paper was not accepted. Subsequently, they wrote to the PNAS, USA where it underwent the usual review process before acceptance. While Siksnys and colleagues lost crucial time in the process, Charpentier and Doudna communicated their findings to the journal Science which accelerated the process of the review and publication thereby enabling them to publish their findings ahead of Siksnys. As in Charpentier and Doudna's work, Siksnys and colleagues also demonstrated that Cas9 cleaves the target DNA, that cleavage specificity is directed by the crRNA sequence, and that the two nuclease domains within Cas9, each cleave one strand. However, the researchers did not notice the crucial importance of tracrRNA for sequence-specific cleavage of target DNA [17].

The impact and application of CRISPR-Cas genome editing technology

Though the in vitro experiments of Charpentier and Doudna, published in 2012, had established the potential of CRISPR-Cas9 for genome editing, the in vivo experimental demonstration was lacking. In the year 2013, two groups achieved the stupendous feat of genome editing in human and mouse cells with CRISPR-Cas9 and independently published the results in the same issue of the journal Science [18,19]. These landmark studies demonstrated that Cas9 nucleases could be directed by crRNA of a defined sequence to induce precise cuts in the genes of mouse and human cells. Since then the application of CRISPR-based genome editing in different organisms has exploded. By simply introducing an engineered sgRNA and the Cas9 nuclease, scientists are now able to make precise changes in the genome (Fig. 3). This has allowed researchers to understand what functions genes do, find out the changes in genes that are associated with disease, introduce new functions into bacteria for biotechnological or industrial applications.

Some of the areas where CRISPR-mediated genome editing technology is beginning to have a tremendous impact is improvement of crops and treatment of genetic diseases like sickle cell disease and b-thalassemia. Recently it has been shown that CRISPR technology can be used to edit gene in human embryos which has raised grave concerns on ethical and social issues. There is a growing recognition that the technology needs to be regulated for responsible use so that social, legal, ethical and scientific challenges arising out of human genome editing can be adequately addressed.

Technology regulation

There is a growing recognition that the technology needs to be regulated for responsible use so that social, legal, ethical and scientific challenges arising out of human genome editing can be adequately addressed.

The CRISPR/Cas9 genetic scissors

When researchers are going to edit a genome using the genetic scissors, they artificially construct a guide RNA, which matches the DNA code where the cut is to be made. The scissor protein, Cas9, forms a complex with the guide RNA, which takes the scissors to the place in the genome where the cut will be made.

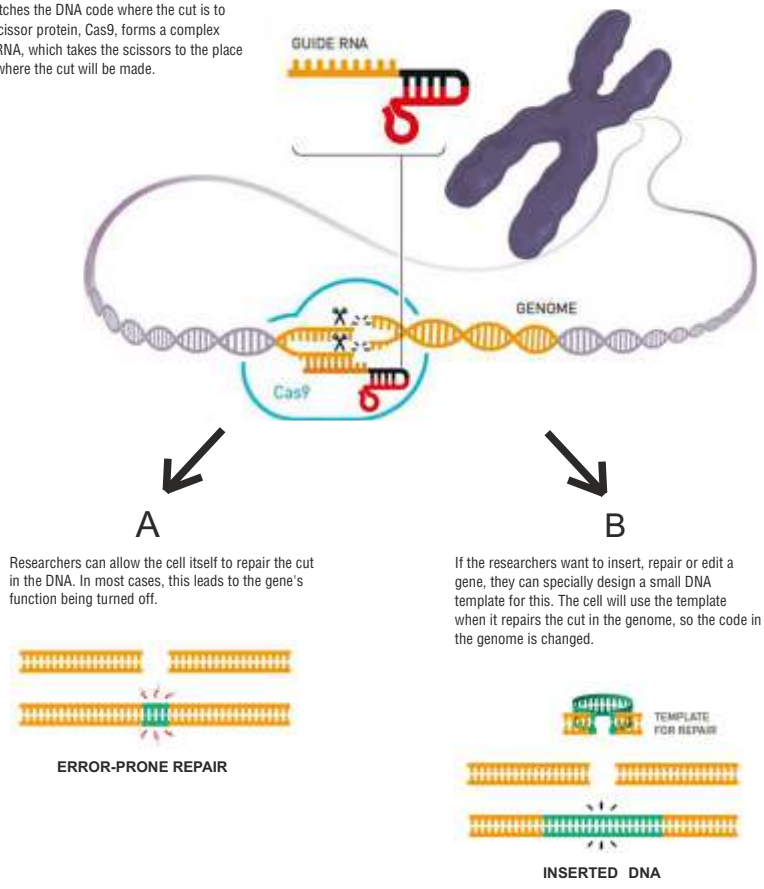

@ Johan Jarnestad/The Royal Swedish Academy of Sciences

Fig. 3: Genome editing with Cas9
The Cas9 enzyme is directed to target DNA by a guide RNA and produces a double-stranded break. The break can be repaired by cellular machinery in an error-prone manner leading to gene knock-out of the function of the gene (A). Or a piece of DNA can be inserted during repair leading to disruption of the gene or replacement of a part (B).

Photo credit @ The Royal Swedish Academy of Science

Reminiscences

Devashish Rath

As I was working on the class 1 CRISPR-Cas system in Escherichia coli during my post-doc tenure at the Uppsala University, Sweden, I had the privilege of interacting with both the Nobel laureates. I visited the laboratory of Dr. Charpentier in Umea University, Sweden in the year 2012 just after the publication of their tracrRNA work. Dr. Charpentier had returned after attending a 'CRISPR conference' in USA and so I had many questions regarding the work presented in the conference. Dr. Charpentier jocularly remarked that "My Swedish friend is very inquisitive". I reminded her that I belonged to India and was in Sweden for a transitory period. It is heart-warming to note that I received a warm welcome in Charpentier lab and had a lively discussion with her and other members of her group. The very next year I met Dr. Doudna, in a 'CRISPR conference' at St. Andrews, Scotland. I was presenting my work on developing a gene silencing application using a type I CRISPR system which immediately attracted the interest of Dr. Doudna as she had recently worked on a similar application using the Cas9 system. In the ensuing discussion she gave me many useful suggestions on enhancing the efficiency of the system. I must acknowledge that I owe these special moments to my then post-doctoral mentor Dr. Magnus Lundgren. While working with the team of Prof. John van der Oost, Dr. Lundgren contributed to seminal work in *E. coli* that provided first molecular insights into the working of the CRISPR-Cas system for which he was a well-recognized name in the CRISPR community.

Acknowledgements:

The author wishes to thank Shri Mandeep Singh, SO/C, AGS, BSG for help with compilation of figures. The author is grateful to Dr. S. K. Ghosh, Ex-Associate Director, BSG, BARC and Dr. G. Ravi Kumar, Head, SIRD and Dr. A.V.S.S.N. Rao, Head, AGS, BSG for their encouragement. The author thanks Dr. Santosh Kumar S., SO/H, RB&HSD for his suggestions to improve the article.

Corresponding Author*

Dr. Devashish Rath (devrath@barc.gov.in)

References

[1] Watson, J.D. and Crick, F.H. "Molecular structure of nucleic acids; a structure for deoxyribose nucleic acid". *Nature*, **171(4356)**, (1953): 737-38.

[2] Knott, G.J. and Doudna,J.A."CRISPR-Cas guides the future of genetic engineering". *Science*, **361(6405)**, (2018): 866-69.

[3] Ishino, Y., et al., "Nucleotide sequence of the iap gene, responsible for alkaline phosphatase isozyme conversion in Escherichia coli, and identification of the gene product". *J Bacteriol,* **169(12)**, (1987): 5429-33.

[4] Mojica, F.J., Juez, G.and Rodriguez-Valera,F."Transcription at different salinities of Haloferax mediterranei sequences adjacent to partially modified PstI sites". *Mol Microbiol*, **9(3)**, (1993): 613-21.

[5] Mojica, F.J., et al., "Biological significance of a family of regularly spaced repeats in the genomes of Archaea, Bacteria and mitochondria". *Mol Microbiol*, **36(1)**, (2000): 244-46.

[6] Jansen, R., et al., "Identification of genes that are associated with DNA repeats in Prokaryotes". *Mol Microbiol*, **43(6)**, (2002):1565-75.

[7] Mojica, F.J., et al., "Intervening sequences of regularly spaced prokaryotic repeats derive from foreign genetic elements". *J Mol Evol*, **60(2)**, (2005): 174-82.

[8] Pourcel, C., Salvignol, G. and Vergnaud, G. "CRISPR elements in Yersinia pestis acquire new repeats by preferential uptake of bacteriophage DNA, and provide additional tools for evolutionary studies". *Microbiology (Reading)*, **151(Pt 3)**, (2005): 653-63.

[9] Bolotin, A., et al., "Clustered regularly interspaced short palindrome repeats (CRISPRs) have spacers of extrachromosomal origin". *Microbiology (Reading)*, **151(Pt 8)**, (2005.): 2551-61.

[10] Barrangou, R., et al., "CRISPR provides acquired resistance against viruses in prokaryotes". *Science*, **315(5819)**, (2007): 1709-12.

[11] Brouns, S.J., et al., "Small CRISPR RNAs guide antiviral defense in prokaryotes". *Science*, **321(5891)**, (2008.): 960-64.

[12] Makarova, K.S., et al., "Evolutionary classification of CRISPR-Cas systems: a burst of class 2 and derived variants". *Nat Rev Microbiol*, **18(2)**, (2020): 67-83.

[13] Bhaya, D., M. Davison, and R. Barrangou, "CRISPR-Cas systems in bacteria and archaea: versatile small RNAs for adaptive defense and regulation". *Annu Rev Genet*, **45**, (2011):273-97.

[14] Terns, M.P. and Terns,R.M. "CRISPR-based adaptive immune systems". *Curr Opin Microbiol*, **14(3)**, (2011): 321-27.

[15] Deltcheva, E., et al., "CRISPR RNA maturation by trans-encoded small RNA and host factor RNase III". *Nature*, **471(7340)**, (2011): 602-7.

[16] Jinek, M., et al., "A programmable dual-RNA-guided DNA endonuclease in adaptive bacterial immunity". *Science*, **337(6096)**, (2012): 816-21.

[17] Gasiunas, G., et al., "Cas9-crRNA ribonucleoprotein complex mediates specific DNA cleavage for adaptive immunity in bacteria". *Proc Natl Acad Sci* U S A, **109(39)**, (2012): E2579-86.

[18] Cong, L., et al., "Multiplex genome engineering using CRISPR/Cas systems". *Science*, **339(6121)**, (2013): 819-23.

Isotope technology in pursuit of water security in India

In the Middle Ganga Plains belonging to Indo-Gangetic Aquifer System, the dominant sources for groundwater recharge, inter-aquifer hydraulic connections, residence time and sustainability of groundwater in various zones have been understood with the aid of isotope indicators.

Tirumalesh Keesari*
Uday Kumar Sinha

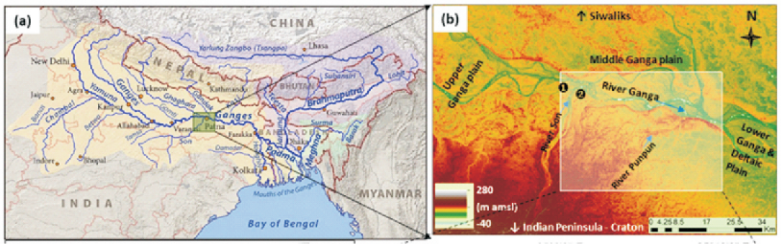

Fig.1: a) Ganga Basin, b) Middle Ganga Plains

Growing water scarcity is a major concern for India and many other developing nations. Irrigation through groundwater pumping has expanded at a very rapid pace in India since 1970s and currently over 60% of the total irrigated area is dependent on groundwater resources. Besides, as high as 85% of the drinking water supplies is met from groundwater. A whopping increase in the bore well construction across India, about twenty-seven million as per current data, obligated the planners to shift strategies from groundwater development to groundwater management. In this regard, a national level action plan was taken up by Central Ground Water Board in the form of "Aquifer Mapping" (CGWB, 2019). Initially studies on aquifer mapping were mainly focussed on geological, hydrogeological and hydrochemical characterization of aquifers techniques. However, it was later realized that tracing groundwater flow paths and assessing groundwater dynamics is quintessential for evaluating the future security of water resources. In this regard, isotope techniques, especially environmental isotopes, have proven to be potential tools in addressing such complex challenges in hydrology.

A pilot isotope study was carried out jointly by Isotope and Radiation Application Division (BARC) and Central Ground Water Board in Bihar State (Patna site). The study region is a part of Middle Ganga Plains (MGP) belonging to Indo-Gangetic Aquifer System, which caters to freshwater needs of several million people in India and Bangladesh. About 28 billion cubic meters (BCM) of groundwater is extracted annually in MGP, amounting to 10% of the India's annual groundwater extraction. Recently, a research paper in Science of the Total Environment has been published providing details on the application of isotope technology for aquifer mapping studies (Keesari *et al.*, 2021).

A total of 120 water samples were collected covering ~550 km^2 area, mostly confining to the Sone-Punpun-Ganga interfluve region (Fig. 1). The isotope information along with available lithological and hydrogeological data helped in achieving the spatial and temporal integration of the groundwater occurring in different depths. The dominant recharge sources for groundwater recharge, interconnection between surface water and groundwater, hydraulic interactions between aquifers, residence time and sustainability of groundwater in various zones have been understood in a precise manner. Isotope indicators not only delineated the groundwater zones based on their dynamisms, but also traced the groundwater flow paths with reference to their sources and origin. This aquifer system starts as a single unit near the southern upland regions located ~ 100 km south of the River Ganga and vertically segregates into different aquifer units.

Three major aquifers are observed with diverse recharge history. The top aquifer (I) is recharged through paleochannels while the intermediate aquifer (II) is being recharged from distant sources and vertical percolation from top aquifer-I is limited. The deep aquifer (III) is very old (~4000 years) and can serve as a strategic future resource in case of any serious crisis (Fig. 2). The inferences from isotope techniques have great bearing on the water security of not only Middle Ganga Plains but also the entire Indo-Gangetic Plains.

The research work discussed in the cited article was conceptualized by Isotope Hydrology Section of Isotope and Radiation Application Division, BARC and carried out in collaboration with Central Ground Water Board, Ministry of Water Resources, Govt. of India.

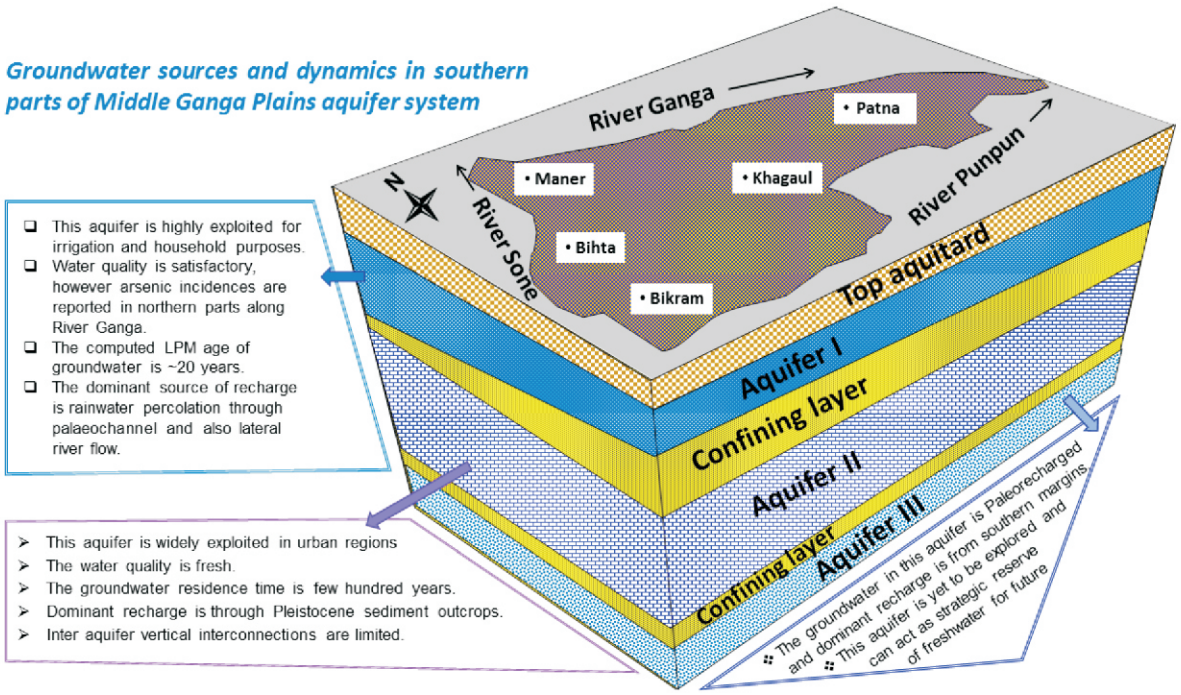

Fig.2: Groundwater distribution, water quality and aquifer dynamics in Southern Part of Middle Ganga Plains, Patna, Bihar.

Corresponding Author*
Tirumalesh Keesari (tirumal@barc.gov.in)

References

[1] CGWB, 2019. *National Compilation on Ground Water Resources of India*, **2017**, Central Ground Water Board, Govt of India available at www.cgwb.gov.in.

[2] Keesari Tirumalesh, Uday Kumar Sinha, Dipankar Saha, S.N. Dwivedi, Rajeev Ranjan Shukla, Hemant Mohokar, Annadasankar Roy, 2021. Isotope systematics of groundwater in central parts of Indo-Gangetic Plain aquifer system, India –implications on deep groundwater sustainability and security, *Science of the Total Environment* **789**, 147860, https://doi.org/10.1016/j.scitotenv.2021.147860.

Heavy steel forgings
for Pressurised Water Reactor program

With the successful completion of this project, India has now acquired the technological know-how and capability to manufacture forgings of thicknesses 350 mm to 750 mm essential to manufacturing of reactor pressure vessel for pressurized water reactor program.

Photo description refer to cover page photo caption

Pressurized Water Reactor (PWR) program requires high purity special grade low alloy steel forgings of relatively large size to manufacture Reactor Pressure Vessel (RPV), a vital and critical component for the plant. The challenging aspects of RPV forging are relatively high thicknesses, maintaining desired chemistry and microstructure coupled with demand for high mechanical properties over entire thickness, good weldability and freedom from hydrogen induced micro-cracks. This involves special technological know-how that needs to be developed through R&D.

With vision for indigenous capability building in heavy thickness RPV forgings, a development project was undertaken successfully at Heavy Engineering Corporation Ltd, Ranchi for small size forgings. Based on experience gained from this project, the next phase of development for heavy forgings (large size and high thickness) was initiated at L&T Special Steels and Heavy Forging Pvt Ltd, Hazira, a joint venture of L&T and NPCIL, considering available infrastructure.

Three prototype scale shell forgings (inner diameter ϕ4.2m and ϕ3.8m) of different thickness were developed successively, with lab scale experiments, industrial scale trials and extensive testing, to progressively improve and optimize the manufacturing processes. The development involved steel melting, refining, vacuum degassing and vacuum casting (control of H, O & N) to produce large size ingots. The ingot is forged to desired shape on a hydraulic press and then subjected to specialized heat treatments multiple times, to achieve the desired metallurgical and mechanical properties. High purity steel was aimed (with very low-level impurity and trace elements) to get superior properties like resistance to embrittlement due to irradiation and thermal ageing. The targeted alloy chemistry for a specific forging thickness was decided based on past experience and prototype trials. Pre-heating of input materials, double degassing and introduction of special prolonged (up to 1000 hours) anti-flaking heat treatment cycles developed at BARC for reducing hydrogen content after forging resulted in control of hydrogen to less than 1 ppm.

Cooling rate at mid-thickness during quenching treatment, an important parameter governing the through thickness properties, was determined for each forging. To establish the heat treatment cycle for each forging having a different mid-thickness cooling rate, BARC developed an innovative technique of lab-scale simulation. Using this technique, the heat treatment parameters were optimized through large number of lab scale trials (~300 trials with ~3000 test specimens), followed by industrial-scale validation before implementing on the prototype forgings.

Ultrasonic testing of these thick forgings was carried out by BARC specialists with stringent sensitivity requirements (100% scanning by normal and angle beam) from all surfaces. Material characterization involves destructive test in all the three directions and five through thickness locations at three orientations at two elevations. This includes mechanical tests (impact toughness & tensile strength) at room temperature and high temperature, drop weight test, fatigue strength evaluation, fracture toughness tests,

P. K. Mishra, Vivek Shrivastav, Rajit Kumar, Harish, R Dinesh Babu, Sujay Bhattacharya from Reactor Projects Group, and R. N. Singh of Materials Group, BARC,Trombay contributed for this article.

metallographic examination and evaluation of thermal embrittlement resistance of steel. Around 2500 test specimens were tested for acceptance of each forging. The quality and properties of the forgings developed meet the acceptance norms of various international codes with high margins.

With successful completion of this project, the country has now acquired the technological know-how and capability to manufacture forgings of thicknesses 350 mm, 550 mm and 750 mm. Specialists of various divisions of BARC and industry worked in tandem in this development and with this, India joins the premier league of very few countries in the world having such capability. It is an important scientific and technological achievement which paves the way for manufacturing capability of RPV forgings required for PWR program. The achievement marks a major step in line with the vision of "Aatmanirbhar Bharat".

The material grade developed is rightfully named "APURVA" (अपूर्व) (**A**dvanced **P**urified **R**eactor **V**essel **A**lloy) considering the nature, scale and importance of this development.

Acknowledgements

S.K. Mohanty, AgS; Arun Kumar, LWRD; Deepak Sharma, LWRD and K. K. Yadav were involved in the implementation of the project.

The project review team included P. Sreenivas, Head, LWRD (retd); Joe Mohan, Head, RPD; S K Jakhotiya, IFA and Himanshu Shankar, Former IFA was helpful in achieving the desired objectives.

Team comprising of G.K. Dey, Former Director, Materials Group; Madangopal Krishnan, Former Director, Materials Group; Rakesh Kumar, Head, IFFF and Rajeev Kapoor, MMD certified overall acceptance of the development.

V.K. Mehra, Director, RPG (retd); Sekhar Basu, Chairman, AEC (retd); R. S. Yadav, Director, RPG (retd); A. B. Mukherjee, Director, RPG (retd); A. K. Mohanty, Director, BARC and K. N. Vyas, Chairman, AEC provided guidance and direction in execution of the project.

IAEA Award for BARC research in **mutation breeding of crops**

The Mutation Breeding Team of Nuclear Agriculture and Biotechnology Division of Bhabha Atomic Research Centre (BARC) has been awarded *Outstanding Achievement Award* by Vienna-headquartered International Atomic Energy Agency (IAEA). The award recognises radiation based mutation research for genetic improvement of crops resulting in the release and notification of 11 varieties – Rice (04), one each in Linseed, Mustard, Cowpea, Urdbean, Pigeonpea, Groundnut and Mungbean – in the last decade.

A total of 49 BARC varieties have been released for commercial cultivation across India so far. These varieties, in addition to improving crop productivity in turn enhancing farm incomes, also uplifted socio-economic status of thousands of farmers, thus contributing positively to the National Food Security Mission.

The award will be delivered during the Side event at the 65th regular session of the IAEA General Conference during 20-24 September 2021.

Young Scientist Award

P. Dhanasekar

Shri P. Dhanasekar of Nuclear Agriculture and Biotechnology Division, BARC has been conferred the *Young Scientist Award* by the IAEA in recognition of his dedicated mutation breeding research leading to the release and notification of 04 high yielding, disease resistant mutant varieties - 03 in pigeonpea and 01 in cowpea – by Government of India for commercial cultivation. The pigeonpea varieties annually garner about 11% of the national breeder seed indent and are widely cultivated by the farmers in central India, which is the hub of pigeonpea cultivation. Further, cowpea mutant variety has the distinction of being India's first summer variety which will augment summer pulse production. Shri Dhanasekar will receive the award during 20-24 September 2021.

Dr. Vikram Sarabhai with Dr. Homi Bhabha

Edited & Published by:
Scientific Information Resource Division
Bhabha Atomic Research Centre, Trombay, Mumbai 400 085, India
BARC Newsletter is also available at URL:http://www.barc.gov.in